Daily and hourly variability in global fire emissions and consequences for atmospheric model predictions of carbon monoxide

M. Mu[1], J.T. Randerson[1], G.R. van der Werf[2], L. Giglio[3], P. Kasibhatla[4], D. Morton[5], G.J. Collatz[5], R.S. DeFries[6], E.J. Hyer[7], E.M. Prins[8], D.W.T. Griffith[9], D. Wunch[10], G.C. Toon[11], V. Sherlock[12], and P.O. Wennberg[10]

1. Department of Earth System Science, Croul Hall, University of California, Irvine, CA, 92697, USA, mmu@uci.edu, jranders@uci.edu
2. Faculty of Earth and Life Sciences, Department of Hydrology and Geo-environmental Sciences, VU University, De Boelelaan 1085, 1081 HV Amsterdam, Netherlands, guido.van.der.werf@falw.vu.nl
3. Department of Geography, LeFrak Hall, University of Maryland, College Park, Maryland, 20742 USA, giglio@hermes.geog.umd.edu
4. Nicholas School of the Environment and Earth Sciences, Box 90328, Duke University, Durham, North Carolina, 27708 USA, psk9@duke.edu
5. NASA Goddard Space Flight Center, Biospheric Sciences Research Code 614.4, Greenbelt, Maryland, 20771 USA, douglas.morton@nasa.gov, george.j.collatz@nasa.gov
6. Department of Ecology, Evolution, and Environmental Biology, Columbia University, 10th Floor Schermerhorn Ext., New York, NY 10027 USA, rd2402@columbia.edu
7. Naval Research Laboratory, Marine Meteorology Division, Monterey, CA 93943 USA, Edward.Hyer@nrlmry.navy.mil
8. UW-Madison Cooperative Institute for Meteorological Satellite Studies - Consultant, Grass Valley, California, 95949, USA, elaine.prins@ssec.wisc.edu
9. University of Wollongong, School of Chemistry, Northfields Ave, New South Wales, 2522, Australia, griffith@uow.edu.au
10. Divisions of Engineering and Applied Science and Geological and Planetary Science, California Institute of Technology, 1200 East California Boulevard, Pasadena, California, 91125, USA, dwunch@caltech.edu, wennberg@gps.caltech.edu
11. Jet Propulsion Laboratory, California Institute of Technology, 4800 Oak Grove Drive Pasadena, California 91109, USA, Geoffrey.C.Toon@jpl.nasa.gov
12. National Institute of Water and Atmospheric Research Ltd., 295-301 Evans Bay Parade, Private Bag 14-901, Kilbirnie, Wellington 6021 New Zealand, v.sherlock@niwa.co.nz

Submitted to:
Journal of Geophysical Research- Atmospheres

4/18/2011

For correspondence:

Mingquan Mu and Jim Randerson (mmu@uci.edu, jranders@uci.edu)
Department of Earth System Science
3317 Croul Hall
University of California, Irvine, CA 92697

Abstract

Attribution of the causes of atmospheric trace gas and aerosol variability often requires the use of high resolution time series of anthropogenic and natural emissions inventories. Here we developed an approach for representing synoptic- and diurnal-scale temporal variability in fire emissions for the Global Fire Emissions Database version 3 (GFED3). We distributed monthly GFED3 emissions during 2003-2009 on a daily time step using Moderate Resolution Imaging Spectroradiometer (MODIS)-derived measurements of active fires from Terra and Aqua satellites. In parallel, mean diurnal cycles were constructed from Geostationary Operational Environmental Satellite (GOES) active fire observations. We found that patterns of daily variability in fires varied considerably across different biomes, with short but intense periods of daily emissions in boreal ecosystems and lower intensity (but more continuous) periods of burning in savannas. On diurnal timescales, our analysis of the GOES active fires indicated that fires in savannas, grasslands, and croplands occurred earlier in the day as compared to fires in nearby forests. Comparison with Total Carbon Column Observing Network (TCCON) and Measurements of Pollution in the Troposphere (MOPITT) column CO observations provided evidence that including daily variability in emissions moderately improved atmospheric model simulations, particularly during the fire season and near regions with high levels of biomass burning. The high temporal resolution estimates of fire emissions developed here may ultimately reduce uncertainties related to fire contributions to atmospheric trace gases and aerosols. Important future directions include reconciling top-down and bottom up estimates of fire radiative power and integrating burned area and active fire time series from multiple satellite sensors to improve daily emissions estimates.

Key words: Global carbon cycle, fire ecology, burn severity, carbon dioxide (CO_2), and atmospheric chemistry

AGU Index terms: 0300 Atmospheric composition and structure, 0400 Biogeosciences, 1600 Global change

1. Introduction

In many parts of the world, fires exhibit considerable variability on timescales of hours to centuries. Understanding the causes of this variability is important for assessing how fires respond to changes in climate and for quantifying how changes in the fire regime influence atmospheric levels of greenhouse gases. Satellite-derived estimates of fire emissions have been shown, for example, to explain some of the interannual variability in atmospheric CH_4 [*van der Werf et al.*, 2004; *Bousquet et al.*, 2006] and CO_2 [*van der Werf et al.*, 2004; *Randerson et al.*, 2005; *Nevison et al.*, 2008] and much of the interannual variability in CO [e.g., *Chen et al.*, 2010]. Concurrent measurements of burned area have improved our understanding of various aspects of ecosystem function, including trajectories of post-fire net primary production [*Hicke et al.*, 2003; *Goetz et al.*, 2006] and surface energy exchange [*Jin and Roy*, 2005; *Lyons et al.*, 2008; *McMillan and Goulden*, 2008]. Motivation for studying higher frequency variability in burned area and emissions– over timescales shorter than one month– comes from another set of inter-related science questions. A key line of inquiry in these studies is the investigation of how diurnal and daily variability in emissions interact with atmospheric transport and chemistry to influence atmospheric composition, radiation, and air quality.

Covariance of emissions with atmospheric transport and chemistry on daily and diurnal timescales can be substantial with important consequences for air quality. Fires in Southern California that occur during periods of Santa Ana winds, for example, have emissions that are often transported in a direction that is largely orthogonal to the mean atmospheric flow [*Moritz et al.*, 2010]. As a consequence, plumes from these fires often extend across urban areas with significant impacts on human health [*Delfino et al.*, 2009]. On diurnal timescales, interactions between the timing of emissions and the growth of the planetary boundary layer (PBL) influence plume dynamics, rates of vertical mixing of aerosols and trace gases, aerosol and trace gas lifetimes, and the lateral transport of these emissions within the free troposphere [*Wang et al.*, 2006; *Chen et al.*, 2009; *Reid et al.*, 2009; *Val Martin et al.*, 2010].

Important aspects of atmospheric chemistry also respond on diurnal timescales, including processes that regulate the formation and destruction of NO, NO_2, and aerosols. Three spectrometers (Global Ozone Monitoring Experiment (GOME), Ozone Monitoring Instrument (OMI), and Scanning Imaging Absorption Spectrometer for Atmospheric Cartography (SCIAMACHY)) on three different satellites currently provide column measurements of NO_2, thus allowing for improved constraints on ozone chemistry and rates of nitrogen deposition in terrestrial and ocean ecosystems. Given the rapid photochemical oxidation of NO_2 during the day [*Boersma et al.*, 2008], use of column measurements in biomass burning regions to infer NO_x fluxes requires an understanding of the diurnal cycle of emissions. For example, *Boersma et al.* [2008] show that across southern Africa, South America, and other tropical regions with high fire emissions, column NO_2 mixing ratios detected by OMI with a 1330 LT overpass are more than 40% higher than similar measurements made by SCIAMACHY with a 1000 LT overpass. This temporal pattern is consistent with high levels of midday fire emissions [e.g., *Giglio*, 2007] that increase the column abundance NO_2 between the two overpass times. The opposite diurnal pattern of column NO_2 is observed over industrial areas where emissions are more uniform during the day and thus NO_2 variations are more closely regulated by the diurnal cycle of loss processes that reach a maximum during midday.

Aerosol models used for climate and air quality assessments [*Chin et al.*, 2009; *Schulz et al.*, 2006] have additional sensitivities to the time interval of fire emissions inventories. Emissions climatologies with coarse time steps (i.e., 1 month) are often distributed within atmospheric models uniformly from day-to-day, increasing the probability that some emissions will be released during precipitation events that occur during the same month. This situation is, of course, unrealistic given the strong controls of precipitation on fuel moisture, ignition, and fire intensity. Failing to account for this temporal mismatch may increase the efficacy of wet deposition and thus create a low bias in aerosol concentrations and lifetimes within the atmospheric model. In this respect, fire emissions are unique compared to many other industrial sources that are mostly decoupled from precipitation levels or drought stress. Although

uncertainties associated with the timing of fire aerosol emissions are likely to be smaller than other factors, including uncertainty associated with condensation and coagulation of organic aerosols and bulk emissions [*Reid et al.*, 2005; *Reid et al.*, 2009], improved daily emissions estimates are needed, nevertheless, to allow for realistic comparisons with satellite and surface aerosol optical depth observations.

Here we describe an approach for representing synoptic and diurnal variability in fire emissions from the Global Fire Emissions Database version 3 (GFED3) monthly time series [*van der Werf et al.*, 2010; *Giglio et al.*, 2010]. Our approach builds on many past studies that have strengthened our understanding of daily and hourly controls of fire emissions and the impact of these emissions on atmospheric chemistry. *Heald et al.* [2003] created one of the first global fire emission inventories with a daily resolution, using Advanced Very High Resolution Radiometer (AVHRR) satellite observations to distribute fire emissions from a monthly climatology developed by *Duncan et al.* [2003]. Use of the polar-orbiting satellite observations at this time step required careful consideration of day-to-day variations in overpass coverage and cloudiness and the impacts of scan angle on the performance of the active fire detection algorithm. Although including diurnal variability in emissions across Asia did not significantly affect CO levels measured in remote aircraft transects over the Pacific, near source regions the impacts on surface CO were substantial. For the North American continent, *Wiedinmyer et al.* [2006] developed a daily 1 km fire emissions time series for 2002-2004 by combining active fire observations from MODIS with high spatial resolution information on vegetation cover (and thus fuel loads and emission factors) from the Global Land Cover (GLC2000) project [*Latifovic et al.*, 2004]. In northern boreal regions, both *Hyer et al.* [2007] and *Chen et al.* [2009] provide evidence that atmospheric simulations of CO are improved when monthly mean emissions time series are replaced by synoptic-scale (weekly) emissions.

Over the past decade, the Fire Locating and Modeling of Burning Emissions (FLAMBE) modeling system also has been used operationally to forecast visibility and air quality at regional to global scales [*Reid et al.*, 2009]. This system integrates active fire measurements from

Geostationary Operational Environmental Satellite (GOES) and polar orbiting (Terra and Aqua) sources with biome-specific fuel loads and emission factors to estimate emissions with an hourly time step. Using FLAMBE emissions with a meso-scale atmospheric model, *Wang et al.* [2006] show that biomass burning plumes from Central America are sometimes transported several hundreds of kilometers north by southerly winds. These plumes have significant effects on air quality and particulate matter concentrations across the south central and south eastern U.S. [*Wang et al.*, 2006] and may intensify severe weather events in the continental interior [*Wang et al.*, 2009].

Diurnal variability in fire activity has been investigated in multiple studies [*Langaas*, 2002; *Prins and Menzel*, 1992; *Eva and Lambin*, 1998; *Giglio*, 2007; *Zhang and Kondragunta*, 2008]. A quantitative understanding of diurnal cycle of fire dynamics is required for comparing estimates of fire radiative power from satellites with different overpass times and sensor characteristics [e.g., *Xu et al.*, 2010] and for modeling plume injection processes [*Freitas et al.*, 2007], in addition to the transport, chemistry and mixing processes described above. Several generalizations emerge from these studies of active fires. First, for most vegetation types, peak fire activity typically occurs during early and mid afternoon (between 1200 and 1600 LT) with fire activity at night often lower by an order of magnitude or more. The drop at night is consistent with lower sensible heat fluxes and wind speeds and higher levels of atmospheric humidity that limit rates of fuel consumption and fire spread rates [e.g., *McRae et al.*, 2005]. Second, diurnal patterns of fire activity vary with biome type, although the results are not always consistent among different studies. For example, croplands tend to have lower levels of burning at night compared to other fire types when analyzed using AVHRR [*Eva and Lambin*, 1998] and GOES [*Zhang and Kondragunta*, 2008] active fire products, but this pattern is not observed in some mixed crop and savanna regions by the Tropical Rain Measuring Mission (TRMM) Visible and InfraRed Scanner (VIRS) [*Giglio*, 2007]. Relationships between diurnal patterns of fire activity and other factors such as spread rate, wind speed, humidity, and fire size have not been systematically investigated. Increasing availability of fire products from multiple geostationary

satellites over the next several years should improve our understanding of these biophysical controls as well as other socio-economic and cultural influences.

Here we develop a global time series of fire emissions at a 0.5° × 0.5° spatial resolution that includes diurnal and synoptic-scale variability by combining information from MODIS and GOES active fire products with a monthly emissions inventory derived from MODIS 500m burned area [*van der Werf et al.*, 2010; *Giglio et al.*, 2010]. We then evaluated the impact of this variability on model estimates of atmospheric CO using Total Carbon Column Observing Network (TCCON) and Measurements of Pollution in the Troposphere (MOPITT) observations. In section 2 below (the methods) we describe key driver datasets, our methodology for developing our high frequency time series, and our modeling approach. In section 3 (the results) we compare our results with available atmospheric observations. In sections 4 and 5 (the discussion and conclusions), we evaluate important sources of uncertainty and identify directions for future investigation.

2. Methods

2.1. Overview

We first describe the datasets and approaches we used to construct our daily and hourly emissions time series. We then provide information about the atmospheric model simulations used to evaluate how monthly, daily, and 3-hourly emissions time series influence our ability to estimate variability in atmospheric CO.

2.2. Global Fire Emissions Database Version 3

GFED3 provides monthly estimates of burned area and carbon emissions during 1997-2009 at a 0.5° spatial resolution. Burned area during 2000-2009 was derived primarily from

500m maps of surface reflectance from the Moderate Resolution Imaging Spectroradiometer (MODIS) on Terra and Aqua satellites using the direct broadcast algorithm from [*Giglio et al.*, 2009]. During times when surface reflectance observations were unavailable, a combination of local regression and regression tree approaches were used to estimate burned area from MODIS active fire observations [*Giglio et al.*, 2010]. These same regression techniques were used to relate TRMM VIRS [*Giglio et al.*, 2003] and Along Track Scanning Radiometer (ATSR) [*Arino and Rosaz*, 1999] active fire observations to MODIS burned area, allowing for the extension of the GFED3 time series prior to the MODIS era (i.e., during 1997-2000). The monthly time-step of GFED3 burned area was determined primarily by the need to temporally aggregate burned area and active fire observations to develop reliable regression models with TRMM and ATSR active fire products.

Carbon emissions from GFED3 were obtained from a biogeochemical model that is driven by the burned area time series described above [*van der Werf et al.*, 2010]. Satellite observations provided important constraints on the spatial distribution of net primary production and fuel loads. Leaf senescence and allocation parameterizations were adjusted to match aboveground biomass observations in savanna and tropical forest ecosystems. Other significant improvements to the biogeochemical model in GFED3 included the use of newly available maps of peatlands in Indonesia to quantify soil organic matter levels, the use of subgrid-scale burned area in different vegetation types to estimate emission factors, and the calibration of a new fire-driven deforestation module using satellite observations of deforestation area. Uncertainty estimates for GFED3 carbon emissions were obtained using a Monte Carlo approach, with error distributions for burned area obtained from *Giglio et al.* [2010] and subjective error distributions assigned for fuel load and combustion completeness components of the model [*van der Werf et al.*, 2010].

2.3. MODIS and GOES active fires

We used MODIS active fire observations to distribute monthly emissions estimates from GFED3 at a daily temporal resolution in 0.5° × 0.5° grid cells. For this, we used collection 5 of the Global Monthly Fire Location Product (MCD14ML) [*Giglio et al.*, 2006] that includes separate lists of active fires for Aqua and Terra. This product contains the individual locations and times of active fires from day and night MODIS overpasses at a 1 km spatial resolution. We screened and removed persistent active fire locations associated with volcanoes, gas flaring, and other non-fire sources using a static hotspot database [*Giglio et al.*, 2006]. In contrast to some of the temporally and spatially aggregated MODIS active fire count products, MCD14ML does not include any corrections for variable cloud cover or gaps in satellite coverage. As described below in section 2.4, we adjusted our approach to take into account latitudinal changes in Aqua and Terra satellite coverage based on comparisons with GOES active time series in the Western Hemisphere.

We used GOES active fire data derived from the Automated Biomass Burning Algorithm (ABBA) [*Prins et al.*, 1998; *Reid et al.*, 2009] to construct climatological mean diurnal cycles of fire activity. We specifically used GOES-11 (west) and GOES-12 (east) observations during 2007-2009 with version 6.0 of the ABBA algorithm. We only used the full hemispheric scans that occurred every three hours from each satellite to build our mean diurnal cycles because these scans were less likely to be affected by rescheduling issues associated with tracking hurricanes and other weather phenomena. We chose these two satellites and time period because of the relatively high saturation temperatures of the 3.9 um channel on these radiometers compared to earlier GOES 10 and GOES 9 instruments. We only used fire pixels for which the retrieval algorithm had higher levels of certainty (classes 0-3), where 0 represented the highest quality in which sub-pixel estimates of fire size and temperature were retrieved from ABBA, 1 represented saturated fire pixels, 2 represented cloud contaminated fire pixels, and 3 represented high probability fire pixels. The spatial resolution of the GOES observations varies, from approximately 4 km at nadir to ~8 km at 60° latitude *[Reid et al.*, 2009].

2.4. Approach for Estimating Daily Fire Emissions Fractions

Within each 0.5° grid cell for which GFED3 monthly emissions were available, we estimated the daily fraction of emissions using the sum of Terra and Aqua active fires. Prior to combining the Terra and Aqua time series, the Terra fire counts were multiplied by a regionally specific factor that was computed as the ratio of mean annual daily Aqua active fires to mean annual daily Terra active fires (Table S1). This adjustment represented an attempt to normalize for regional differences in the diurnal cycle of fire activity as sampled by Terra (10:30am/10:30pm) as compared to Aqua (1:30pm/1:30am). For most regions, these factors were greater than 1 which meant that by applying the adjustment factor Terra active fires were amplified – giving this time series proportionally greater weight because of the lower probability of observing fires in mid-morning as compared to early afternoon [e.g., *Giglio*, 2007]. Agreement between this adjusted sum and GOES active fires was relatively high in boreal forests across Alaska and Canada, in western forests in the U.S., and in dry tropical forests in southern Mexico (Figure 1). Correlations were also high in South America across Bolivia and Brazilian states of Rondonia, Mato Grosso, and Tocantins. The relationship between MODIS and GOES was weaker in the easternmost states of Brazil, in northern Mexico and across the southeastern U.S.

As a consequence of satellite orbital geometry, coverage by Aqua and Terra increased toward the poles, reducing the size of spatial gaps between successive overpasses. In the tropics, these gaps created an artificial spikiness in the distribution of active fires that had the potential to bias estimates of daily emissions (Figure S1). By smoothing the MODIS active fire time series in each 0.5° grid cell using 3-day and 5-day center mean filters, correlation between the MODIS time series and GOES active fires increased in the tropics, particularly between 15°N and 15°S (Figure 2). In contrast, in mid and high latitudes where there were fewer gaps in coverage by MODIS (and there was less evidence for spikiness as shown in Figure S2), smoothing degraded the correlation with GOES.

To account for the latitudinal differences in MODIS coverage, we generated our daily fraction of emissions using a 3-day center mean smoothing filter equator-ward of 25°N and 25°S and no smoothing filter pole-ward of these latitudes. Thus our daily emissions fractions represented a true 1-day time step in the extra-tropics, and ~3 day time step in the tropics and subtropics. We opted to accept this lower resolution for the tropics and subtropics of the Western Hemisphere where hourly GOES observations were available to allow for a consistent treatment across the tropics as a whole by MODIS. As the availability of active fire observations from other geostationary satellites increases in the future [e.g., *Reid et al.*, 2009], we expect refinements to this approach and significant reductions in uncertainties associated with daily emissions estimates in tropical Africa and Asia.

Following the approach described above, we generated a time series of daily fire fractions for each month in the GFED3 time series during 2003-2009, each with a variable number of days corresponding to the length of each month (i.e., Jan = 31, Feb = 28, etc). Each year these time series had 365 days, with the exception of leap years (2004 and 2008) that had 366 days with one extra day in February.

2.5. Approach for Estimating 3-Hourly Fire Emissions Fractions

We constructed climatological mean diurnal cycles of fire activity from GOES active fire observations, as a function of vegetation type and region using all available GOES satellite observations from full hemisphere scans during 2007-2009. We then created a set of eight 3-hourly fractions of emissions for each 0.5° grid cell and month, using sub-grid scale information on burned area in different vegetation types to weight the contribution of different diurnal cycles to the grid cell mean during each month.

To construct mean diurnal cycles of fire activity from measurements spanning multiple time zones, we used the following method. GOES active fire observations had a Greenwich Mean Time (GMT/UTC) time stamp associated with them. We converted these UTC time

stamps to local solar time (LST) at each grid cell by using the following equation: LST = UTC + longitude/15.

Mean diurnal cycles of GOES active fires for different regions and vegetation types in the Western Hemisphere, normalized to the same daily sum, are shown in Figure 3. The corresponding absolute levels of active fires observed for each region and vegetation type are shown in Figure S3. These mean diurnal cycles were constructed only from 0.05° areas within each region that had greater than 80% coverage of one of the three aggregated vegetation types: forests, shrublands and savannas, or croplands and grasslands. We used the Terra MODIS version 4 MOD12C1 land cover product [*Friedl et al.*, 2002] to identify these areas, and derived our aggregated vegetation types from the International Geosphere Biosphere Program (IGBP) classification within this product. Specifically, we included the IGBP classes of evergreen needleleaf forest, evergreen broadleaf forest, deciduous needleleaf forest, deciduous broadleaf forest, and mixed forest in our aggregated forest class, closed and open shrubland, woody savannas, and savannas in our aggregated shrubland and savanna class, and grasslands, croplands, cropland/natural vegetation mosaic, and barren or sparsely vegetated areas in our grassland and cropland class. Our logic was to broadly separate vegetation types into three classes as a function of high, medium and low fuel densities. The distribution of burned area in these three aggregated vegetation types is summarized in Figures S4 and S5 and Table 1 for different continental scale regions shown in Figure S6.

To develop our global product, we applied the normalized diurnal fractions for the 3 different vegetation classes from GOES (Figure 3) to regions with roughly similar biogeography. For example, we used normalized diurnal fractions from boreal North America in boreal Asia. The complete mapping is provided in Table 2.

2.6. Atmospheric model simulations

To simulate atmospheric CO we used the GEOS-Chem global three-dimensional model of tropospheric chemistry [*Bey et al.*, 2001] which was driven by assimilated meteorological observations from the Goddard Earth Observation System (GEOS) of the NASA Global Modeling and Assimilation Office (GMAO). We used version 8-01-02 of the model (http://acmg.seas.harvard.edu/geos/) driven by GEOS-5 reanalysis [*Rienecker et al.*, 2008] that had 72 vertical layers and was averaged to a 2° × 2.5° horizontal resolution. The new GEOS-5 reanalysis used a modified relaxed Arakawa-Schubert convection scheme [*Ott et al.*, 2009] that led to improvements in the distribution of precipitation and atmospheric circulation across the tropics as compared to GEOS 4.

Our model simulations spanned the 2004 to 2009 period, after a spin up period of one year. For the spin-up, we used 2004 meteorology and monthly, daily or hourly fire emissions from 2003. In these simulations, we carried separate tracers for monthly GFED3 CO emissions and the daily and hourly emissions time series described above. We saved 3-hourly distributions of CO from the model, and sampled the three-dimensional distribution of CO at the time and location of the MOPITT satellite measurements and TCCON stations as described below.

In addition to the fire emissions tracers described above, we also included CO emissions from anthropogenic, biofuel and biogenic emissions in the GEOS-Chem model simulations. The sources of fossil fuel emissions were from *Streets et al.* [2006]. Biofuel emissions were from the inventory of *Yevich and Logan* [2003]. Biogenic sources were multi-year annual cycle mean (2004-2009) generated from the latest Model of Emissions of Gases and Aerosols from Nature driven by GEOS5 meteorology (MEGAN) [*Guenther et al.*, 2006]. All CO simulations used the same monthly 3-D OH concentration fields archived from a GEOS-Chem full-chemistry simulation [*Fiore et al.*, 2003].

2.7. Atmospheric Observations

We compared our GEOS-Chem model simulations with TCCON CO observations from six sites: Park Falls, Lamont, JPL, Darwin, Wollongong, and Lauder. We selected these six sites based on the length of the available time series (longer than one year during the period of 2004-2009) and the requirement that fire-emitted CO visibly contribute to some of the observed variability of column CO at the different stations based on our monthly mean simulations with GEOS-Chem. This effectively excluded stations near urban areas with the exception of JPL. We used the beta version of the public TCCON data archive (http://tccon.ipac.caltech.edu/). TCCON is a global network of ground-based and sun-viewing Fourier Transform Infrared (FTIR) spectrometers designed to measure column abundances of CO, CO_2, CH_4, N_2O and other molecules that absorb in the near infrared [*Wunch et al.*, 2011]. Within the network, stringent requirements on the instrumentation, data processing and calibration have improved the accuracy and precision of the measurements [*Wunch et al.*, 2011]. Past work with TCCON observations has led to an identification of biases in vertical mixing in atmospheric models [*Yang et al.*, 2007], improved estimates of CH_4 emissions from the city of Los Angeles [*Wunch et al.*, 2009], reduced uncertainties associated with emission factors from savanna fires [*Paton-Walsh et al.*, 2010] and new diagnostics of the magnitude of seasonal carbon exchange in temperate and boreal ecosystems [*Keppel-Aleks et al.*, 2010]. TCCON retrievals of CO have been calibrated against in situ aircraft profiles at three sites: Lamont, Lauder, and Park Falls, and the calibration coefficient determined from these three sites is applied to all TCCON CO data [*Wunch et al.*, 2010]. Based on these comparisons, the estimated TCCON CO column dry air molar fractions have an accuracy of ± 4 ppbv. Averaging kernels for CO peak in the upper troposphere/lower stratosphere such that the sensitivity to CO at 100 hPa is more than double that at the surface [*Wunch et al.*, 2010].

To compare the model with the observations, we first averaged all the column CO observations together within each 3-hour interval of model output. We also computed the mean solar zenith angle (SZA) of the observations within each interval, and used this mean SZA with a

look up table of averaging kernels (e.g., Figure S7) to estimate the column CO from GEOS-Chem.

We also compared our simulations with the MOPITT version 4 daily level 3 CO product [*Deeter et al.*, 2003; *Emmons et al.*, 2004]. Improvements in the MOPITT version 4 product included a finer vertical resolution, a floating surface level, a log-normal distribution for CO volume mixing ratio (VMR) variability, and CO prior that varied spatially and temporally [*Deeter*, 2009]. To compare with our model simulations, we only used daytime MOPITT observations, sampling the model during the 10:30am MOPITT overpass time. We only included level 3 observations in our analysis for which the degree of freedom was greater than 0.98. We used MOPITT averaging kernels and priors to construct the model CO column following the instructions for MOPITT version 4 dataset [*Deeter*, 2009]. We did not compare our model simulations with surface CO observations because long-term time series of daily measurements were not available for many sites.

3. Results

3.1. Daily and 3-Hourly Fire Emissions for Individual Grid Cells

Figures 4 and 5 show examples of original monthly GFED3 emissions, daily emissions, and hourly emissions derived using the approach described in sections 2.4, and 3-hourly time series described in section 2.5 for 0.5° grid cells from South America and Alaska. For South America we show a representative grid cell from the northeastern corner of the Brazilian state of Mato Grosso during 2007, an area that has undergone extensive deforestation over the last decade. In this region, fires are often used to clear forests for mechanized agriculture and pasture [*Morton et al.*, 2008]. They also are used, to a lesser degree, to maintain forage quality in existing pastures, although most of the emissions are associated with forest clearing [*van der*

Werf et al., 2009]. For this cell, much of the burning occurred during a single period in late August and early September.

For Alaska we show a grid cell that was partly burned during the summer of 2009 as a part of the Minto Flats South fire. Measurements from within fire perimeters that burned during 2004 in Alaska yielded a mean fire combustion rate of 3300 g C per m^2 of burned area with a range of 1500-4600 g C per m^2 of burned area [*Boby et al.*, 2010]. Mean fuel consumption levels from GFED3 for this 2009 fire were somewhat higher but within the reported range: 3607 g C per m^2 of burned area for the grid cell shown in the figure. The active fire observations indicated that almost all of the burning in this grid cell occurred during July and the first week of August, with the most intense period of burning occurring during the first week of July. For both grid cells, the distribution of burning within the growing season was modified considerably by using active fires to distribute fire emissions on a daily basis.

3.2. Global Patterns of Daily Fires

Global patterns of daily fires have the potential to provide new information about fire type and ecosystems processes. Key metrics of daily fire activity varied considerably among different biomes (Figure 6). The mean number of fire days each year, for example, ranged between 5-20 in many boreal ecosystems to over 100 in many savanna regions of South America and Africa (Figure 6a). The number of fire events each year, defined as the number of continuous periods of fire activity, also was higher in savannas (4-25 events) compared to boreal forests (2-6 events) but the relative difference between these two biomes was smaller than for the number of fire days (Figure 6b). As a result, the number of fire days per event was considerably higher in savannas compared to boreal forests (Figure 6c).

It is important to note that these patterns are scale dependent (and were generated here at the 0.5° spatial resolution of GFED3). They also were influenced by the 3-day center mean smoothing we applied to active fires in tropical regions. Nevertheless, the relative spatial

distributions suggested several interesting features of global fire behavior. The small number of days per fire event in boreal regions, for example, provided evidence that these fires were short-lived but intense given the relatively high levels of fuel consumption typical for this biome (Table 3). In contrast, the large number of fire days and large number of days per fire event in savanna regions indicated a more continuous pattern of burning over the fire season. Additional 500m burned area information on fire sizes would be required to assess whether this pattern in savannas was driven by multiple independent small fires (of short duration) or a smaller number of large fires that moved slowly across the landscape.

Agricultural fires also had a unique signature as quantified using these metrics. Across the Southeastern U.S., central Asia, southern China, fires in these regions were characterized by a high number of individual fire events each year (Figure 6b) and a very low duration for each event (1-2 days) (Figure 6c).

Estimates of daily rates of burned area and fire emissions, derived from mean annual burned area and emissions from van der Werf *et al.* [2010] and the number of fire days per year described above were broadly consistent with biome-level differences described above (Figure 7). Daily rates of emissions from fires in boreal regions per unit of burned area (daily rates of fuel consumption) were more than 70 times higher than in African savannas (Table 3).

3.3. Hemispheric Patterns of 3-Hourly Fires

Most fire activity occurred in the middle of the day and this was especially the case for Central and South America where 35% – 56% of all fires in different biome types occurred during the 3-hour interval between 12:00-15:00 LT. In contrast, the least amount fire activity in all regions and biome types occurred after midnight, between 0:00-09:00 LT, with the sum during this 9 hour interval never exceeding 13% of the 24-hour total (Figure 3).

The smallest diurnal amplitudes of fire activity occurred in forest and shrub biomes of North America. Fires in these biomes had considerably higher levels of burning in late afternoon

and evening relative to fires in other regions and ecosystems (Figure 3). This shift in the diurnal cycle is consistent with longer duration fires and thus stronger controls on fire spread rates from synoptic-scale meteorological events that persist for multiple days [e.g., *French et al.*, 2011]. Forest and shrubland biomes in boreal North America had similar diurnal patterns of fire activity. This was consistent with the MODIS-derived land cover classification we used that assigned areas with lower levels of evergreen tree cover (e.g., taiga) to shrub and savanna classes.

In Central and South America, small differences in phase were visible between the timing of forest fires relative to shrubland/savanna and cropland/grassland fires (Figure 3). Fires in the latter two biome classes started increasing earlier in the morning and often tapered off at earlier times in the afternoon. One possible mechanism explaining this pattern is that crop, grass and shrub fuels dry out faster than forest fuels, enabling land managers to start the ignition process earlier in the day [*Giglio,* 2007]. This explanation is consistent with observations that show intact tropical forest canopies have higher levels of surface humidity that are known to inhibit fire activity [*Nepstad et al.*, 2004]. Higher levels of fuels in forests also may enable longer periods of burning that persist into late afternoon and evening.

3.4. Impacts of temporal resolution of emissions on atmospheric CO simulations

At TCCON stations, model simulations indicated that fires contributed to some of the observed variability in CO on synoptic to interannual timescales (Figure 8). At Darwin, for example, fire-derived CO was a dominant contributor to the annual cycle, with mixing ratios peaking during the moderate 2006 El Nino. At Park Falls, in contrast, fire contributions were smaller and occurred primarily during mid-summer. Increasing the temporal resolution of fire emissions modestly improved the agreement between the model and the observations at Darwin and Park Falls, particularly when we replaced monthly with daily emissions and analyzed contributions to variability during the peak fire season (Table 4). At Darwin, using daily

emissions instead of monthly emissions increased the correlation between the model and the observations from 0.48 to 0.53. During the fire season, the improvements were larger, with the correlation increasing from 0.71 to 0.80 (Figure 9). At other TCCON stations, use of daily emissions instead of monthly emissions had relatively small or virtually no impact on model performance. Further, use of 3-hourly emissions did not significantly improve model performance beyond that obtained from the daily emissions time series at all of these sites.

We conducted a similar analysis using daily level-3 MOPITT4 observations over a set of broad geographic regions. Small improvements in model performance occurred using daily instead of monthly emissions in many regions, including boreal North America, temperate North America, southern hemisphere South America, boreal Asia, Southeast Asia, equatorial Asia, and Australia (Table 5). Higher temporal frequency emissions had almost no effect on model performance in several other regions, including Central America, northern hemisphere South America, and the Middle East. As with the TCCON sites, improvements gained from the use of higher frequency emissions were larger on sub-seasonal timescales (and during peak fire season).

The largest improvements in model performance derived from using daily fire emissions estimates occurred over source regions or in nearby outflow regions (Figure 10). Daily emissions increased the correlation between model and MOPITT 4 observations considerably in boreal North America and Asia, southern Africa, India, Myanmar, and northern Australia. As expected, in areas far removed from source regions like the mid-Pacific, the impacts of using higher frequency emissions were minimal. This was probably a consequence of substantial atmospheric mixing that attenuated high frequency variability originating from continental source regions.

4. Discussion

High temporal resolution estimates of fire emissions, like the time series we developed here, may allow for more effective attribution of the sources of trace gases and aerosols. This is possible because in many regions fires are often sporadic, creating unique spatial and temporal

imprints on atmospheric constituents that, in turn, provide a means for quantifying levels of fire emissions and isolating these contributions from other sources [e.g., *Wang et al.*, 2006]. High temporal resolution estimates of fire emissions also are important for carbon data assimilation systems that often integrate CO_2 observations with other meteorological variables on hourly time scales [*Peters et al.*, 2007; *Zupanski et al.*, 2007]. In addition, daily emissions estimates are needed for air quality studies in regions with high fuel loads near population centers, such as efforts to quantify the human health impacts of peat fires during 2010 across Russia.

One important direction for future research is to reconcile top-down estimates of fire radiative power (FRP) and fire radiative energy (FRE) derived from spectrometer data [*Wooster et al.*, 2005; *Roberts and Wooster*, 2008] with bottom-up estimates of energy release from forward biogeochemical models. Figure 7, where we estimated the daily rate of carbon emissions, is a step in this direction. It shows, for example, that boreal fires tend to have significantly higher rates of emissions per day of burning than savanna fires. Since the energy content of most fuels varies within a relatively narrow range, total burned area and fuel consumption provide a strong constraint on the total energy released by a fire. Active fires from polar orbiting and geostationary sources, in turn, allow for the partitioning of this energy through time, including diurnally, thus allowing for more reasonable forward model estimates of energy release. In this context, the north-south gradients of daily rates of carbon emissions reported here for North American forests appear qualitatively consistent with fire plume heights measured by *Val Martin et al.* [2010]. Both plume heights and daily emissions were at maximum levels in boreal forests in Alaska and Canada, at intermediate levels in temperate forests and shrublands across the U.S., and at minimum levels for tropical forests in southern Mexico, Guatemala, and other countries in northern Central America. Mechanistically, fires that release high levels of carbon each day also would be expected to generate the energy required to inject plumes to higher altitudes within the free troposphere [*Frietas et al.*, 2007]. Conversely, deeper and drier atmospheric boundary layers in boreal regions may create conditions that simultaneously enable both higher rates of fuel consumption and higher plumes. A more direct comparison of FRE from

forward modeling and satellite-derived approaches will require several additional steps however, including, for example, the availability of emission data with the same spatial resolution as the active fire data (~ 1 km) and careful consideration of the length and structure of the fire front.

Future improvements in high temporal resolution time series of fire emissions will likely come from several sources, including use of additional satellite observations and consideration of additional fire processes. Burned area estimates derived from surface reflectance changes in many instances can provide daily-to-weekly estimates of the location of the fire front [*Tansey et al.*, 2008]. Combining this information with the active fire time series described above has the potential to reduce uncertainties. Importantly, with moderate resolution (e.g., ~ 500m) burned area data, it may be possible to interpolate the movement of the fire perimeter over a period of several days- thus filling in gaps created by clouds or intervals between successive satellite overpasses. On diurnal time scales, it may be possible to relate the amplitude of the diurnal cycle to key environmental variables such as wind speed, humidity, and fuel moisture. Here we assumed that total carbon and CO emissions were the same– as a first approximation. We hypothesize that reduced gas production is proportionally higher at night (relative to CO_2 emissions) because of higher levels of atmospheric humidity and lower wind speeds that tend to suppress flaming stages of combustion. Testing this hypothesis will require the use of new continuous gas analyzers for CO_2, CH_4, and CO in field studies and/or the deployment of space-based laser spectrometers that measure multiple gases, following for example from mission concepts such as Active Sensing of Carbon Dioxide Emissions over Nights, Days and Seasons (ASCENDS).

Sources of uncertainty

Using a global atmospheric model, here we observed modest improvements in our simulations when we included daily and hourly variability in emissions. There are probably at

least four different reasons why the model improvements were not larger. First, even if emissions were known perfectly, other sources of error within the atmospheric modeling framework would be expected to limit simulation performance. For example, we did not use high temporal resolution inventories for several other important sources of CO, including fossil fuel emissions, because these time series are not yet available at a global scale. Uncertainties in several other sources, including biogenic emissions of volatile organic compounds, also are considerable and our understanding of seasonal and interannual controls on these fluxes remain poorly understood. In addition, significant uncertainties exist with respect to several aspects of atmospheric model transport, including for example vertical mixing by convection in the free troposphere, flow in regions with complex terrain, and atmospheric boundary layer dynamics. The relatively coarse resolution of our atmospheric model (2.5°) also probably damped temporal and spatial variability in simulated atmospheric CO driven by our daily and hourly emissions time series.

Second, at several of the TCCON sites, mostly notably Lamont and Lauder, the contribution from local fire sources was most likely relatively small. Long-range atmospheric transport, including at Lauder transport of CO from fires in Australia, southern Africa, and South America, is likely to act as a low-pass smoothing filter on emissions as a consequence of diffusive mixing, thus limiting improvements in the model obtained from replacing monthly with daily (or hourly) fire emissions.

Third, important uncertainties remain with respect to quantifying daily variability in emissions. The MODIS active fire time series used here was derived from polar-orbiting Terra and Aqua satellites and as a consequence, gaps in coverage existed in tropical regions. It is likely this source of uncertainty will be substantially reduced in future as more geostationary satellite observations of active fires become publicly available for Africa and Asia [*Reid et al.*, 2009], along with more detailed information on fire radiative power and fire size. Even with the expected future increases in data availability, persistent cloud cover in tropical regions will remain an important challenge with respect to active fire detection and thus the development of a daily time series of fires driven by either geostationary or polar-orbiting satellite observations.

Fourth, on longer time scales our understanding of several of the key processes regulating emissions remains limited. One exception is burned area. Over the last decade, improved change detection algorithms and increased availability of high quality moderate resolution surface reflectance data has transformed our understanding of burned area at a global scale and has led to a several-fold reduction in uncertainty, particularly in boreal forest and savanna biomes. In contrast, our ability to quantify and develop realistic parameterization of fuel consumption and emission factors has not progressed as quickly, in part from dearth of information on how to scale estimates of tree mortality and combustion completeness across heterogeneous landscapes in savanna, woodland, and tropical forest ecosystems [e.g., *van der Werf et al.*, 2010]. Further, some fires in forests and agricultural areas may be too small to detect with moderate resolution surface reflectance data, particularly in agricultural ecosystems and in tropical forests.

On hourly time-scales, one primary driver of uncertainty is related to diurnal variations in the performance of the active fire detection algorithm. For the 4 μm band, the thermal contrast between fire pixels and neighboring cells is highest at night when the surface is cool and there is no contamination from reflected solar radiation [*Giglio*, 2007]. As a result, the efficacy of the active fire detection algorithm may be higher, particularly for smaller fires. Lower detection efficiencies during the day, when there is less thermal contrast, may lead to an overall reduction in the amplitude of the diurnal cycle. Cooler air and surface temperatures at night, however, also may reduce the likelihood of false detections (which would mostly likely occur during midday) causing a bias in the opposite direction [*Giglio*, 2007]. In this context, evaluating the robustness of the diurnal cycles measured here in different plant functional types (and the relatively small differences in phasing) will require comparisons with other geostationary active fire products, the use of other land cover maps, and more detailed analysis of diurnal changes in the efficiency of the ABBA algorithm used here.

5. Conclusions

Here we developed an approach for representing daily and hourly variability in global fire emissions using a combination of polar-orbiting and geostationary satellite observations of active fires. Outside of the tropics, our time series resolved day-to-day variations in fires. In the tropics, we applied a 3-day center mean smoothing filter to avoid spikiness caused by gaps in coverage by Aqua and Terra satellites. For each month, we constructed a mean diurnal cycle of fire activity in each grid cell based on burned area in different vegetation types and vegetation-specific mean diurnal cycles derived from GOES observations. Our time series was designed for use in global atmospheric studies of trace gases and aerosols. Because of the sporadic nature of fires on synoptic time scales in many regions, high temporal resolution estimates may allow for improved attribution of causes of variations in atmospheric constituents.

Several distinct biome-level differences in fire behavior emerged from our study of daily fires. In boreal biomes, the number of fire days in a given year at a 0.5° spatial resolution rarely exceeded 20 whereas in tropical savannas this often exceeded 100. The duration of fire events (continuous periods of burning) also was shorter in boreal biomes. The abrupt nature of boreal fires, combined with high levels of fuel consumption (g C per m^2 of burned area) caused daily rates fuel consumption to be over an order of magnitude higher in boreal regions than in savanna regions. Diurnally, observations from GOES indicated that fires in grasslands, savannas, and crops often occurred earlier in the day than in forests.

Atmospheric model simulations with daily and 3-hourly emissions generally showed improved agreement with ground based and space based remote sensing observations of CO, particularly during the fire season. Directions for future research include reconciling forward model and satellite-derived estimates of fire radiative power and integrating multiple geostationary and polar orbiting fire products to produce higher quality (and higher temporal resolution) emissions time series.

Acknowledgements

This research was supported by NASA grants NNX08AF64G and NNX10AT83G and the EU Seventh Research Framework Programme (MACC project, contract number 218793). The time series described here is publicly available on the Global Fire Emissions Database server (www.globalfiredata.org). We thank E. Lyons for contributing to the development of the daily fire emissions time series. Dr. Hyer acknowledges support from the NASA Interdisciplinary Studies Program. U.S. funding for TCCON comes from NASA's Terrestrial Ecology Program (NNX08A186G), the Orbiting Carbon Observatory Program (NAS7-03001), the DOE/ARM Program and the Atmospheric CO_2 Observations from Space Program. Some of the research described in this paper was performed at the Jet Propulsion Laboratory, California Institute of Technology, under a contract with the National Aeronautics and Space Administration. The Lauder TCCON measurements were funded by New Zealand Foundation for Research, Science and Technology contracts CO1X0204 and CO1X0406. We thank B. Connor for work establishing the Lauder FTIR time series and J. Robinson for contributions to the Lauder CO time series.

References

Arino, O., and J.-M. Rosaz (1999), 1997 and 1998 world ATSR fire atlas using ERS-2 ATSR-2 data, paper presented at Proceedings of the Joint Fire Science Conference and Workshop, University of Idaho and the International Association of Wildland Fire, Boise, Idaho.

Bey, I., D. J. Jacob, R. M. Yantosca, J. A. Logan, B. D. Field, A. M. Fiore, Q. B. Li, H. G. Y. Liu, L. J. Mickley, and M. G. Schultz (2001), Global modeling of tropospheric chemistry with assimilated meteorology: Model description and evaluation, *J. Geophys. Res.-Atmos.*, *106*(D19), 23073-23095.

Boby, L. A., E. A. G. Schuur, M. C. Mack, D. Verbyla, and J. F. Johnstone (2010), Quantifying fire severity, carbon, and nitrogen emissions in Alaska's boreal forest, *Ecological Applications*, *20*(6), 1633-1647.

Boersma, K. F., D. J. Jacob, H. J. Eskes, R. W. Pinder, J. Wang, and R. J. van der A (2008), Intercomparison of SCIAMACHY and OMI tropospheric NO2 columns: Observing the diurnal evolution of chemistry and emissions from space, *J. Geophys. Res.-Atmos.*, *113*(D16), D16S26, doi:10.1029/2007jd008816.

Bousquet, P., et al. (2006), Contribution of anthropogenic and natural sources to atmospheric methane variability, *Nature*, *443*(7110), 439-443.

Chen, Y., J. T. Randerson, G. R. van der Werf, D. C. Morton, M. M., and P. S. Kasibhatla (2010), Nitrogen deposition in tropical forests from savanna and deforestation fires, *Global Change Biology*, *16*(7), 2024-2038, doi:2010.1111/j.1365-2486.2009.02156.x.

Chen, Y., Q. Li, J. T. Randerson, E. A. Lyons, R. A. Kahn, D. L. Nelson, and D. J. Diner (2009), The sensitivity of CO and aerosol transport to the temporal and vertical distribution of North American boreal fire emissions, *Atmos. Chem. Phys.*, *9*(17), 6559-6580.

Chin, M., T. Diehl, O. Dubovik, T. F. Eck, B. N. Holben, A. Sinyuk, and D. G. Streets (2009), Light absorption by pollution, dust, and biomass burning aerosols: a global model study and evaluation with AERONET measurements, *Annales Geophysicae*, *27*(9), 3439-3464.

Deeter, M. N. (2009), MOPITT (Measurements of Pollution in the Troposphere) Provisional Version 4: Product User's Guide, MOPITT Algorithm Development Team, Atmosphere Chemistry Division, National Center for Atmospheric Research, Boulder, Corolado.

Deeter, M. N., et al. (2003), Operational carbon monoxide retrieval algorithm and selected results for the MOPITT instrument, *J. Geophys. Res.-Atmos.*, *108*(D14), 4399, doi:4310.1029/2002jd003186.

DeMore, W. B., S. P. Sander, D. M. Golden, R. F. Hampson, M. J. Kurylo, C. J. Howard, A. R. Ravishankara, C. E. Kolb, and M. J. Molina (1997), Chemical kinetics and photochemical data for use in stratospheric modeling, NASA Panel for Data Evaluation: JPL Publication 97-4, Jet Propul. Lab., Pasadena, Calif., 278pp.

Delfino, R. J., et al. (2009), The relationship of respiratory and cardiovascular hospital admissions to the southern California wildfires of 2003, *Occup. Environ. Med.*, *66*(3), 189-197.

Duncan, B. N., R. V. Martin, A. C. Staudt, R. Yevich, and J. A. Logan (2003), Interannual and seasonal variability of biomass burning emissions constrained by satellite observations, *J. Geophys. Res.-Atmos.*, *108*(D2), 4100, doi:4110.1029/2002jd002378.

Emmons, L. K., et al. (2004), Validation of Measurements of Pollution in the Troposphere (MOPITT) CO retrievals with aircraft in situ profiles, *J. Geophys. Res.-Atmos.*, *109*(D3), D03309, doi:03310.01029/02003jd004101.

Eva, H., and E. F. Lambin (1998), Remote sensing of biomass burning in tropical regions: Sampling issues and multisensor approach, *Remote Sensing of Environment*, *64*(3), 292-315.

Fiore, A. M., et al. (2003), Variability in surface ozone background over the United States: Implication for air quality policy, *J. Geophys. Res.*, *108*(D24), 4787, doi:10.1029/2003JD003855.

Freitas, S. R., K. M. Longo, R. Chatfield, D. Latham, M. Dias, M. O. Andreae, E. Prins, J. C. Santos, R. Gielow, and J. A. Carvalho (2007), Including the sub-grid scale plume rise of vegetation fires in low resolution atmospheric transport models, *Atmos. Chem. Phys.*, *7*(13), 3385-3398.

French, N. H. F. et al. (2011), Model comparisons for estimating carbon emissions from North American wildland fire. *J. Geophys. Res.*, doi:10.1029/2010JG001469, in press.

Friedl, M. A., et al. (2002), Global land cover mapping from MODIS: algorithms and early results, *Remote Sensing of Environment*, *83*(1-2), 287-302.

Giglio, L. (2007), Characterization of the tropical diurnal fire cycle using VIRS and MODIS observations, *Remote Sensing of Environment*, *108*(4), 407-421.

Giglio, L., J. D. Kendall, and R. Mack (2003), A multi-year active fire dataset for the tropics derived from the TRMM VIRS, *Int. J. Remote Sens.*, *24*(22), 4505-4525.

Giglio, L., I. Csiszar, and C. O. Justice (2006), Global distribution and seasonality of active fires as observed with the Terra and Aqua Moderate Resolution Imaging Spectroradiometer (MODIS) sensors, *Journal of Geophysical Research-Biogeosciences*, *111*(G2), G02016, doi:02010.01029/02005jg000142.

Giglio, L., T. Loboda, D. P. Roy, B. Quayle, and C. O. Justice (2009), An active-fire based burned area mapping algorithm for the MODIS sensor, *Remote Sensing of Environment*, *113*(2), 408-420.

Giglio, L., J. T. Randerson, G. R. van der Werf, P. S. Kasibhatla, G. J. Collatz, D. C. Morton, and R. S. DeFries (2010), Assessing variability and long-term trends in burned area by merging multiple satellite fire products, *Biogeosciences*, *7*(3), 1171-1186.

Goetz, S. J., G. J. Fiske, and A. G. Bunn (2006), Using satellite time-series data sets to analyze fire disturbance and forest recovery across Canada, *Remote Sensing of Environment*, *101*(3), 352-365.

Guenther, A., T. Karl, P. Harley, C. Wiedinmyer, P. I. Palmer, and C. Geron (2006), Estimates of global terrestrial isoprene emissions using MEGAN (Model of Emissions of Gases and Aerosols from Nature), *Atmos. Chem. Phys.*, *6*, 3181-3210.

Heald, C. L., D. J. Jacob, P. I. Palmer, M. J. Evans, G. W. Sachse, H. B. Singh, and D. R. Blake (2003), Biomass burning emission inventory with daily resolution: Application to aircraft observations of Asian outflow, *J. Geophys. Res.-Atmos.*, *108*(D21), 8811, doi:8810.1029/2002jd003082.

Hicke, J. A., G. P. Asner, E. S. Kasischke, N. H. F. French, J. T. Randerson, G. J. Collatz, B. J. Stocks, C. J. Tucker, S. O. Los, and C. B. Field (2003), Postfire response of North American boreal forest net primary productivity analyzed with satellite observations, *Global Change Biology*, *9*(8), 1145-1157.

Hyer, E. J., E. S. Kasischke, and D. J. Allen (2007), Effects of source temporal resolution on transport simulations of boreal fire emissions, *J. Geophys. Res.-Atmos.*, *112*(D1), D01302, doi:01310.01029/02006jd007234.

Jin, Y., and D. P. Roy (2005), Fire-induced albedo change and its radiative forcing at the surface in northern Australia, *Geophys. Res. Lett.*, *32*(13), L13401, doi:13410.11029/12005gl022822.

Keppel-Aleks, G., P. O. Wennberg, and T. Schneider (2010), Sources of variations in total column carbon dioxide, *Atmos. Chem. Phys. Discuss.*, *10*, 30569-30611.

Langaas, S. (2002), Temporal and spatial distribution of savanna fires in Senegal and the Gambia, West Africa, 1989-1990, derived from multi-temporal AVHRR night images, *International Journal of Wildland Fire*, *2*(1), 21-36.

Latifovic, R., Z. L. Zhu, J. Cihlar, C. Giri, and I. Olthof (2004), Land cover mapping of north and central America - Global Land Cover 2000, *Remote Sensing of Environment*, *89*(1), 116-127.

Lyons, E. A., Y. F. Jin, and J. T. Randerson (2008), Changes in surface albedo after fire in boreal forest ecosystems of interior Alaska assessed using MODIS satellite observations, *Journal of Geophysical Research-Biogeosciences*, *113*(G2), G02012, doi:02010.01029/02007jg000606.

McMillan, A. M. S., and M. L. Goulden (2008), Age-dependent variation in the biophysical properties of boreal forests, *Global Biogeochemical Cycles*, *22*(2), Gb2019, doi:2010.1029/2007gb003038.

McRae, D. J., J. Z. Jin, S. G. Conard, A. I. Sukhinin, G. A. Ivanova, and T. W. Blake (2005), Infrared characterization of fine-scale variability in behavior of boreal forest fires, *Can. J. For. Res.-Rev. Can. Rech. For.*, *35*(9), 2194-2206.

Moritz, M. A., T. J. Moody, M. A. Krawchuk, M. Hughes, and A. Hall (2010), Spatial variation in extreme winds predicts large wildfire locations in chaparral ecosystems, *Geophys. Res. Lett.*, *37*, L04801, doi:04810.01029/02009gl041735.

Morton, D. C., R. S. Defries, J. T. Randerson, L. Giglio, W. Schroeder, and G. R. van Der Werf (2008), Agricultural intensification increases deforestation fire activity in Amazonia, *Global Change Biology*, *14*(10), 2262-2275.

Nepstad, D. et al. (2004), Amazon drought and its implications for forest flammability and tree growth: a basin-wide analysis, *Global Change Biology*, *10*, 704-717.

Nevison, C. D., N. M. Mahowald, S. C. Doney, I. D. Lima, G. R. Van der Werf, J. T. Randerson, D. F. Baker, P. Kasibhatla, and G. A. McKinley (2008), Contribution of ocean, fossil fuel, land biosphere, and biomass burning carbon fluxes to seasonal and interannual variability in

atmospheric CO2, *Journal of Geophysical Research-Biogeosciences*, *113*(G1), G01010, doi:01010.01029/02007jg000408.

Ott, L. E., J. Bacmeister, S. Pawson, K. Pickering, G. Stenchikov, M. Suarez, H. Huntrieser, M. Loewenstein, J. Lopez, and I. Xueref-Remy (2009), Analysis of convective transport and parameter sensitivity in a single column version of the Goddard Earth Observation System, Version 5, general circulation model, *Journal of Atmospheric Sciences*, *66*, 627-645.

Paton-Walsh, C. et al. (2010), Trace gas emissions from savanna fires in northern Australia, *J. Geophys. Res.-Atmos.*, *115*, D16314, 16310.11029/12009jd013309.

Peters, W., et al. (2007), An atmospheric perspective on North American carbon dioxide exchange: CarbonTracker, *Proceedings of the National Academy of Sciences of the United States of America*, *104*(48), 18925-18930.

Prins, E. M., and W. P. Menzel (1992), Geostationary satellite detection of biomass burning in South-America, *Int. J. Remote Sens.*, *13*(15), 2783-2799.

Prins, E. M., J. M. Feltz, W. P. Menzel, and D. E. Ward (1998), An overview of GOES-8 diurnal fire and smoke results for SCAR-B and 1995 fire season in South America, *J. Geophys. Res.-Atmos.*, *103*(D24), 31821-31835.

Randerson, J. T., G. R. van der Werf, G. J. Collatz, L. Giglio, C. J. Still, P. Kasibhatla, J. B. Miller, J. W. C. White, R. S. DeFries, and E. S. Kasischke (2005), Fire emissions from C-3 and C-4 vegetation and their influence on interannual variability of atmospheric CO_2 and delta(CO_2)-C-13, *Global Biogeochemical Cycles*, *19*(2), Gb2019, doi:2010.1029/2004gb002366.

Reid, J. S., R. Koppmann, T. F. Eck, and D. P. Eleuterio (2005), A review of biomass burning emissions part II: intensive physical properties of biomass burning particles, *Atmos. Chem. Phys.*, *5*, 799-825.

Reid, J. S., et al. (2009), Global monitoring and forecasting of biomass-burning smoke: Description of and lessons from the Fire Locating and Modeling of Burning Emissions (FLAMBE) program, *IEEE Journal of Selected Topics in Applied Earth Observations and Remote Sensing*, *2*(3), 144-162.

Rienecker, M.M, M.J. Suarez, R. Todling, J. Bacmeister, L. Takacs, H.-C. Liu, W. Gu, M. Sienkiewicz, R.D. Koster, R. Gelaro, I. Stajner, and E. Nielsen (2008), The GEOS-5 Data Assimilation System - Documentation of Versions 5.0.1, 5.1.0, and 5.2.0, *Technical Report Series on Global Modeling and Data Assimilation*, NASA/TM-2008-104606, Vol. 27, 118pp.

Roberts, G. J., and M. J. Wooster (2008), Fire detection and fire characterization over Africa using Meteosat SEVIRI, *IEEE Trans. Geosci. Remote Sensing*, *46*(4), 1200-1218.

Schulz, M., et al. (2006), Radiative forcing by aerosols as derived from the AeroCom present-day and pre-industrial simulations, *Atmos. Chem. Phys.*, *6*, 5225-5246.

Streets, D. G., Q. Zhang, L. Wang, K. He, J. Hao, Y. Wu, Y. Tang, and G. R. Carmichael (2006), Revisiting China's CO emissions after the Transport and Chemical Evolution over the Pacific (TRACE-P) mission: Synthesis of inventories, atmospheric modeling, and observations, J. Geophys. Res., 111, D14306, doi:10.1029/2006JD007118.

Tansey, K., J. M. Gregoire, P. Defourny, R. Leigh, J. F. O. Pekel, E. van Bogaert, and E. Bartholome (2008), A new, global, multi-annual (2000-2007) burnt area product at 1 km resolution, *Geophys. Res. Lett.*, *35*, L01401, doi:01410.01029/02007gl031567.

Val Martin, M., J. A. Logan, R. A. Kahn, F. Y. Leung, D. L. Nelson, and D. J. Diner (2010), Smoke injection heights from fires in North America: analysis of 5 years of satellite observations, *Atmos. Chem. Phys.*, *10*(4), 1491-1510.

van der Werf, G. R., D. C. Morton, R. S. DeFries, L. Giglio, J. T. Randerson, G. J. Collatz, and P. S. Kasibhatla (2009), Estimates of fire emissions from an active deforestation region in the southern Amazon based on satellite data and biogeochemical modelling, *Biogeosciences*, *6*(2), 235-249.

van der Werf, G. R., J. T. Randerson, G. J. Collatz, L. Giglio, P. S. Kasibhatla, A. F. Arellano, S. C. Olsen, and E. S. Kasischke (2004), Continental-scale partitioning of fire emissions during the 1997 to 2001 El Nino/La Nina period, *Science*, *303*(5654), 73-76.

van der Werf, G. R., et al. (2010), Global fire emissions and the contribution of deforestation, savanna, agricultural, forest, and peat fires (1997-2008), *Atmospheric Chemistry and Physics Discussions*, *10*, 16153-16230.

Wang, J., S. C. van den Heever, and J. S. Reid (2009), A conceptual model for the link between Central American biomass burning aerosols and severe weather over the south central United States, *Environmental Research Letters*, *4*(1).

Wang, J., S. A. Christopher, U. S. Nair, J. S. Reid, E. M. Prins, J. Szykman, and J. L. Hand (2006), Mesoscale modeling of Central American smoke transport to the United States: 1. "Top-down" assessment of emission strength and diurnal variation impacts, *J. Geophys. Res.-Atmos.*, *111*(D5), D05s17, doi:10.1029/2005jd006416

Wiedinmyer, C., B. Quayle, C. Geron, A. Belote, D. McKenzie, X. Y. Zhang, S. O'Neill, and K. K. Wynne (2006), Estimating emissions from fires in North America for air quality modeling, *Atmospheric Environment*, *40*(19), 3419-3432.

Wooster, M. J., G. Roberts, G. L. W. Perry, and Y. J. Kaufman (2005), Retrieval of biomass combustion rates and totals from fire radiative power observations: FRP derivation and calibration relationships between biomass consumption and fire radiative energy release, *J. Geophys. Res.-Atmos.*, *110*(D24), D24311, doi:24310.21029/22005jd006318.

Wunch, D., P. O. Wennberg, G. C. Toon, G. Keppel-Aleks, and Y. G. Yavin (2009), Emissions of greenhouse gases from a North American megacity, *Geophys. Res. Lett.*, *36*, L15810, doi:15810.11029/12009gl039825.

Wunch, D. et al. (2010), Calibration of the Total Carbon Column Observing Network using aircraft profile data, *Atmospheric Measurement Techniques*, *3*, 1351-1362.

Wunch, D., G. C. Toon, J. -F. L. Blavier, R. A. Washenfelder, J. Notholt, B. J. Connor, D. W. T. Griffith, V. Sherlock, P. O. Wennberg (2011). The Total Carbon Column Observing Network. *Phil. Trans. R. Soc. A-issue* (2011) 369, doi:10.1098/rsta.2010.0240.

Xu, W., M. J. Wooster, G. Roberts, and P. Freeborn (2010), New GOES imager algorithms for cloud and active fire detection and fire radiative power assessment across North, South and Central America, *Remote Sensing of Environment, 114*(9), 1876-1895.

Yang, Z., R. A. Washenfelder, G. Keppel-Aleks, N. Y. Krakauer, J. T. Randerson, P. P. Tans, C. Sweeney, and P. O. Wennberg (2007), New constraints on Northern Hemisphere growing season net flux, *Geophys. Res. Lett.*, *34*(12), L12807, doi:12810.11029/12007gl029742.

Yevich, R., and J. A. Logan (2003), An assessment of biofuel use and burning of agricultural waste in the developing world, *Global Biogeochemical Cycles*, *17*(4), 1095, doi:1010.1029/2002gb001952.

Zhang, X. Y., and S. Kondragunta (2008), Temporal and spatial variability in biomass burned areas across the USA derived from the GOES fire product, *Remote Sensing of Environment*, *112*(6), 2886-2897.

Zupanski, D., A. S. Denning, M. Uliasz, M. Zupanski, A. E. Schuh, P. J. Rayner, W. Peters, and K. D. Corbin (2007), Carbon flux bias estimation employing maximum likelihood ensemble filter (MLEF), *J. Geophys. Res.-Atmos.*, *112*(D17), D17107, doi:17110.11029/12006jd008371.

Tables

Table 1. Fraction of burned area in different aggregated vegetation classes during 2003-2009.

Region[1]	Forests	Shrublands and savannas	Croplands and grasslands
BONA[2]	0.558	0.400	0.042
TENA	0.239	0.311	0.450
CEAM	0.327	0.360	0.312
NHSA	0.109	0.618	0.272
SHSA	0.199	0.643	0.158
EURO	0.177	0.323	0.500
MIDE	0.016	0.273	0.710
NHAF	0.053	0.800	0.147
SHAF	0.075	0.875	0.049
BOAS	0.295	0.394	0.311
CEAS	0.029	0.062	0.909
SEAS	0.225	0.356	0.419
EQAS	0.783	0.145	0.072
AUST	0.027	0.897	0.076

1. Abbreviations for the different regions are as follows: boreal North America (BONA), temperate North America (TENA), Mexico and Central America (CEAM), northern hemisphere South America (NHSA), southern hemisphere South America (SHSA), Europe (EURO), the Middle East (MIDE), northern hemisphere Africa (NHAF), southern hemisphere Africa (SHAF), boreal Asia (BOAS), central Asia (CEAS), Southeast Asia (SEAS), equatorial Asia (EQAS), and Australia and Oceania (AUST). A spatial map of the distribution of these regions is given in Figure S6.

2. The MODIS land cover product classified open taiga forests in boreal North America and boreal Asia as open shrubland, and in some instances, savanna. These ecosystems are very different from subtropical savanna and shrublands, with one notable difference being the presence of large stores of carbon in organic soils that are vulnerable to combustion.

Table 2. Mapping of regions in the Western Hemisphere to other parts of the world for the purpose constructing diurnal cycles of fire emissions.

Western Hemisphere (GOES observations available)		Rest of World (diurnal cycles constructed from GOES obs. in corresponding Western Hemisphere regions)
Boreal North America (BONA)	->	Boreal Asia (BOAS)
Temperate North America (TENA)	->	Europe (EURO) and Central Asia (CEAS)
Central America and Mexico (CEAM)	->	Middle East (MIDE)
Northern Hemisphere South America (NHSA)	->	Northern Hemisphere Africa (NHAF)
Southern Hemisphere South America (SHSA)	->	Southeast Asia (SEAS), Equatorial Asia (EQAS), Southern Hemisphere Africa (SHAF), and Australia and Oceania (AUST)

Table 3. Summaries for (a) mean annual burned area (Mha/yr) (b) Mean annual fire emissions (Tg C/yr); (c) fuel consumption (g C per m^2 of burned area); (d) numbers of fire days per year; (e) daily rates of burned area (% of annual burned area/day); (f) daily rates of fuel consumption (g C/m^2 of burned area/day) averaged during 2003-2009.

Region	Mean annual burned area (Mha/yr)	Mean annual emissions (Tg C/yr)	Fuel consumption (g C per m^2 of burned area)	Number of fire days (days/yr)	% of annual burned area per day	Daily rates of fuel consumption (g C per m^2 of burned area per day)
BONA	2.3	64	2764	7.2	13.9	383
TENA	1.6	10	621	10.5	9.5	59
CEAM	1.3	18	1442	54.5	1.8	26
NHSA	2.3	22	966	75.8	1.3	13
SHSA	17.7	299	1692	51.6	1.9	33
EURO	0.6	4	660	9.4	10.6	70
MIDE	0.9	2	206	12.6	7.9	16
NHAF	120.0	447	372	86.1	1.2	4
SHAF	126.8	570	449	95.1	1.1	5
BOAS	6.2	110	1762	10.2	9.8	173
CEAS	13.6	34	249	15.9	6.3	16
SEAS	7.6	106	1383	43.7	2.3	32
EQAS	1.1	116	10677	42.5	2.4	251
AUST	39.8	121	305	28.4	3.5	11
Global sum or mean:	341.7	1922	1682	38.8	5.3	78

Table 4. Correlation coefficients between TCCON CO column observations and GEOS-Chem simulations with monthly, daily and 3-hourly fire emissions (mean annual cycle not removed)

TCCON station	Latitude		Full time series			Peak fire season (3 months)		
			Monthly	Daily	3-hourly	Monthly	Daily	3-hourly
Park Falls, WI	45.945N	90.273W	0.26	0.29	0.29	0.13	0.25	0.24
Lamont, OK	36.604N	97.486W	0.13	0.14	0.13	0.42	0.47	0.44
JPL, CA	34.200N	118.180W	0.27	0.29	0.33	0.54	0.56	0.56
Darwin, AU	12.424S	130.892E	0.48	0.53	0.53	0.71	0.80	0.82
Wollongong, AU	34.406S	150.879E	0.59	0.60	0.60	0.53	0.56	0.56
Lauder, NZ	45.038S	169.684E	0.67	0.67	0.67	0.54	0.56	0.56

Table 5. Correlation between MOPITT column CO and GEOS-Chem model simulations with monthly, daily, and 3-hourly fire emissions

Region	Full time series[1]			Peak fire season (3 months)		
	Monthly	Daily	3-hourly	Monthly	Daily	3-hourly
BONA	0.44	0.50	0.50	0.32	0.41	0.42
TENA	0.45	0.47	0.47	0.19	0.23	0.23
CEAM	0.02	0.02	0.02	0.38	0.40	0.40
NHSA	0.18	0.18	0.18	0.26	0.25	0.25
SHSA	0.50	0.52	0.52	0.58	0.61	0.61
EURO	0.68	0.68	0.68	0.36	0.40	0.40
MIDE	0.32	0.32	0.32	-0.07	-0.06	-0.06
NHAF	0.29	0.30	0.30	0.32	0.33	0.33
SHAF	0.62	0.64	0.64	0.60	0.63	0.63
BOAS	0.56	0.59	0.59	0.60	0.65	0.65
CEAS	0.50	0.51	0.51	0.27	0.29	0.29
SEAS	0.44	0.46	0.45	0.43	0.46	0.46
EQAS	0.46	0.48	0.48	0.65	0.70	0.70
AUST	0.53	0.55	0.55	0.54	0.59	0.59

1. Correlations from 1° × 1° grid cells that had more than 50 valid daily MOPITT 4 observations during 2004-2009 were averaged in each region between 70°N and 50°S.

Figure captions

Figure 1. Correlation of daily active fire counts from GOES and the sum of Aqua and Terra sensors during 2007-2009. Active fires from Terra were first adjusted using the regional factors shown in Table S1 to account for differences in satellite overpass times (relative to Aqua) that have consequences for sampling the diurnal cycle of fire activity. We only included in the analysis grid cells and years that had at least 10 GOES active fire observations and 10 Aqua or Terra observations.

Figure 2. a) Zonal sums of GFED3 fire emissions for 5° latitude bands (Tg C/yr) and annual mean active fire counts from GOES and the sum of Aqua and Terra MODIS during 2007-2009 in the Western Hemisphere. b) Zonal mean correlation coefficients between daily GOES active fires and the sum of Aqua and Terra active fires (with overpass adjustments to Terra) for three different levels of smoothing: no smoothing, a 3-day centered mean smoothing filter, and a 5-day centered mean smoothing filter. In both panels, active fires from Terra were first adjusted using the regional factors shown in Table S1 to normalize for differences in satellite overpass times (relative to Aqua).

Figure 3. Diurnal cycles of fires based for 3-hour intervals using GOES active fire counts. The different diurnal cycles were constructed only using grid cells at a 0.05°×0.05° resolution each within region that had 80% or more coverage by each vegetation type. The fire counts have been normalized so that the sum for each individual vegetation type equaled 1 over a 24-hour period.

Figure 4. a) Monthly GFED3 emissions averaged over a single 0.5 grid cell in northern South America (11.75° S, 51.75° W) during 2007. This grid cell was located in the northeastern corner of the Brazilian state of Mato Grosso. Daily emissions (b) and 3-hourly emissions (c) for the same grid cell derived using the approach described in the text.

Figure 5. Same as Figure 4 but for a 0.5° grid cell in interior Alaska (64.75° N, 149.75° W) during 2009.

Figure 6. Global annual mean distribution of a) the number of fire days per year, b) the number of fire events per year, and c) the number of fire days per fire event. These maps were generated using the daily fire fraction time series described in the main text (section 2.4) during 2003-2009. Panel c was constructed by dividing panel (a) by panel (b). A fire event was defined as a single continuous period for which the daily fire fraction time series was non-zero. This meant that at least one Aqua or Terra active fire observation existed for that day in the extra-tropics (north of 25°N and south of 25°S), and the same for the tropics, but with a 3-day center-mean smoothing applied to compensate for gaps in satellite coverage. In the construction of panels (a) and (b), if a grid cell did not have any fires in a given year, this year was excluded from the multi-year mean shown in the figure.

Figure 7. a) Mean annual burned area (kha/yr), b) mean burned area per fire day (kha/day), c) mean annual fire emissions ($gC/m^2/yr$) and d) mean annual emissions per day of burning (g $C/m^2/day$). All panels show mean patterns during 2003-2009. If a grid cell did not have any fires in a given year, this year was excluded from the multi-year mean shown in the figure.

Figure 8. CO column observations and model estimates of the fire contribution to each column observation at: a) Park Falls, b) Lamont, c) JPL, d) Darwin, e) Wollongong and f) Lauder. Black dots show the 3-hourly TCCON observations. Red dots show the MOPITT 4 daily level 3 satellite observations. The model simulations of fire-derived CO are from GEOS-Chem with monthly emissions (blue line) and daily emissions (dark green line). Total CO column estimates from the model with daily fire emissions (light green line) are also shown in the figure. Simulations with 3-hourly emissions were very similar to those with daily emissions and thus are not shown. The MOPITT 4 observations shown here were transformed using the TCCON averaging kernels.

Figure 9. Model vs. observed column CO for the Darwin, Australia TCCON site sampled during 3 month intervals during peak fire season each year. a) Monthly fire emissions model estimates, b) daily fire emissions model estimates, and c) 3-hourly fire emissions model estimates. Units are column dry air mole fractions of CO $\times 10^9$ (ppb).

Figure 10. Improvements in model performance obtained from using daily and 3-hourly emissions estimates. The difference in model correlation with MOPITT4 daily level 3 observations is shown for model simulations with daily and monthly emissions (a) and 3-hourly and daily emissions (b). Prior to estimating the correlation between the model and MOPITT4, a monthly mean annual cycle of CO was removed from both the observations and the model.

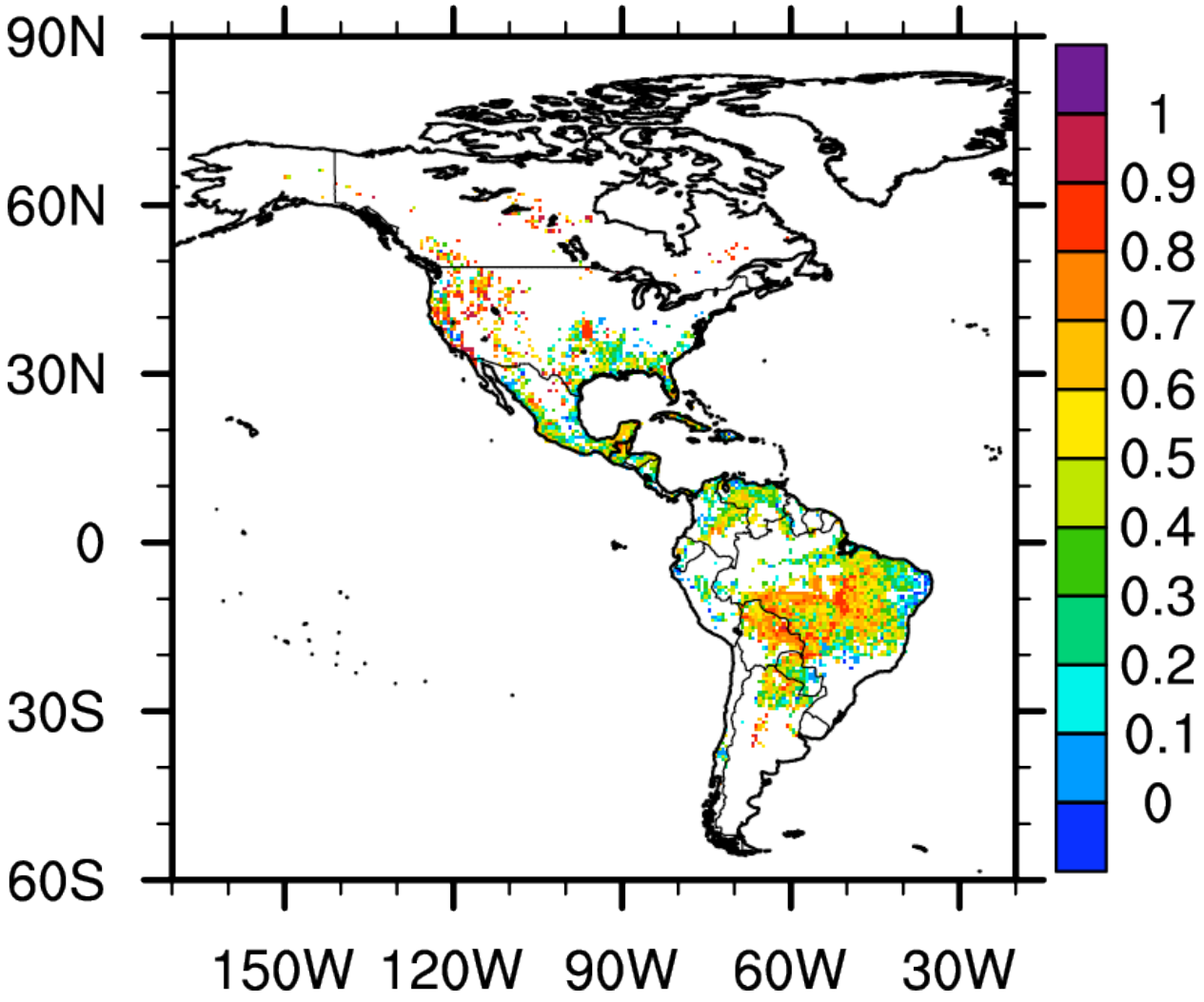
90N
60N
30N
0
30S
60S
150W
120W
90W
60W
30W
1
0.9
0.8
0.7
0.6
0.5
0.4
0.3
0.2
0.1
0

Figure 1.

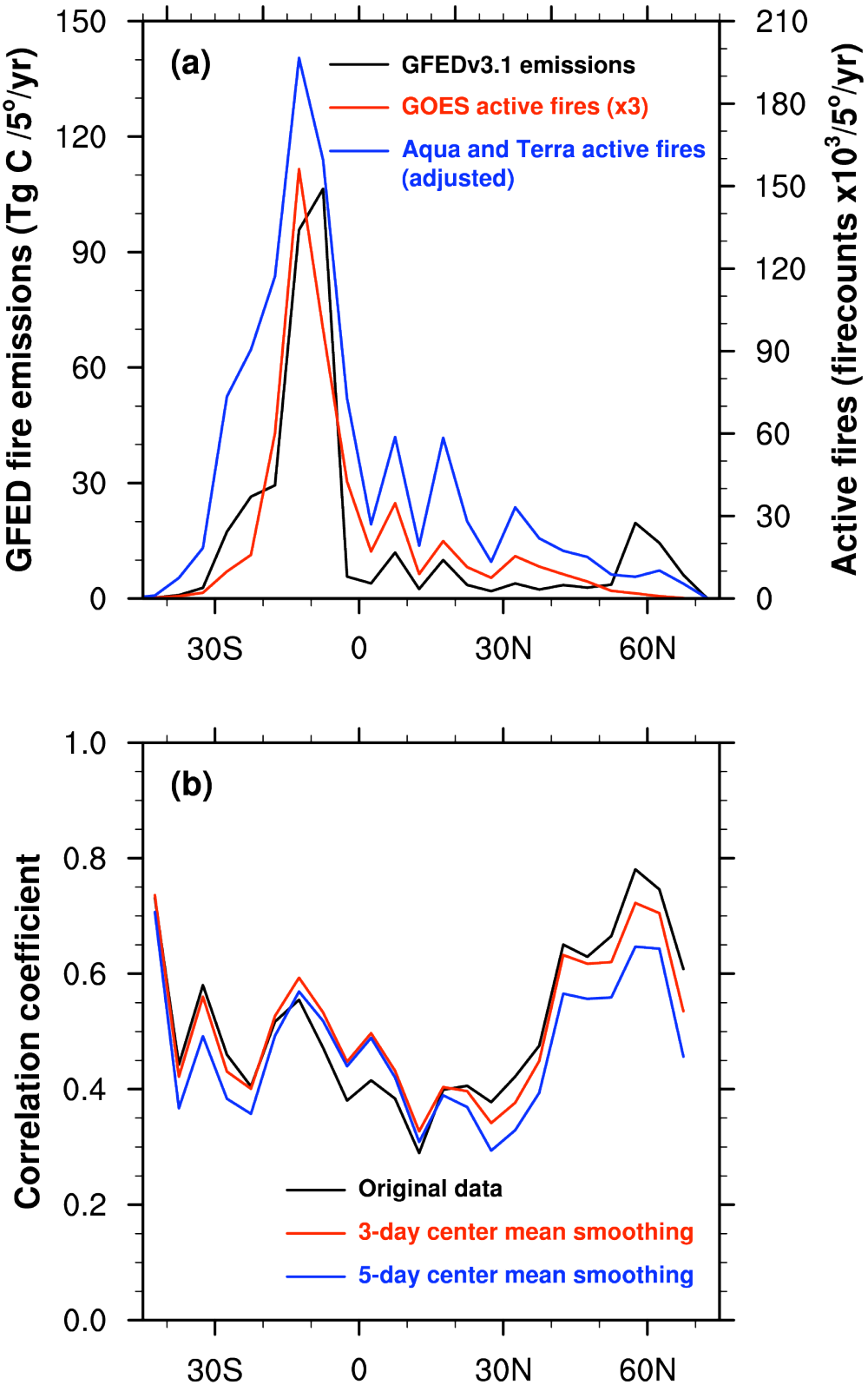
(a)
GFEDv3.1 emissions
GOES active fires (x3)
Aqua and Terra active fires (adjusted)
GFED fire emissions (Tg C /5°/yr)
Active fires (firecounts x10³/5°/yr)
150
120
90
60
30
0
210
180
150
120
90
60
30
0
30S
0
30N
60N
(b)
Correlation coefficient
1.0
0.8
0.6
0.4
0.2
0.0
Original data
3-day center mean smoothing
5-day center mean smoothing
30S
0
30N
60N

Figure 2.

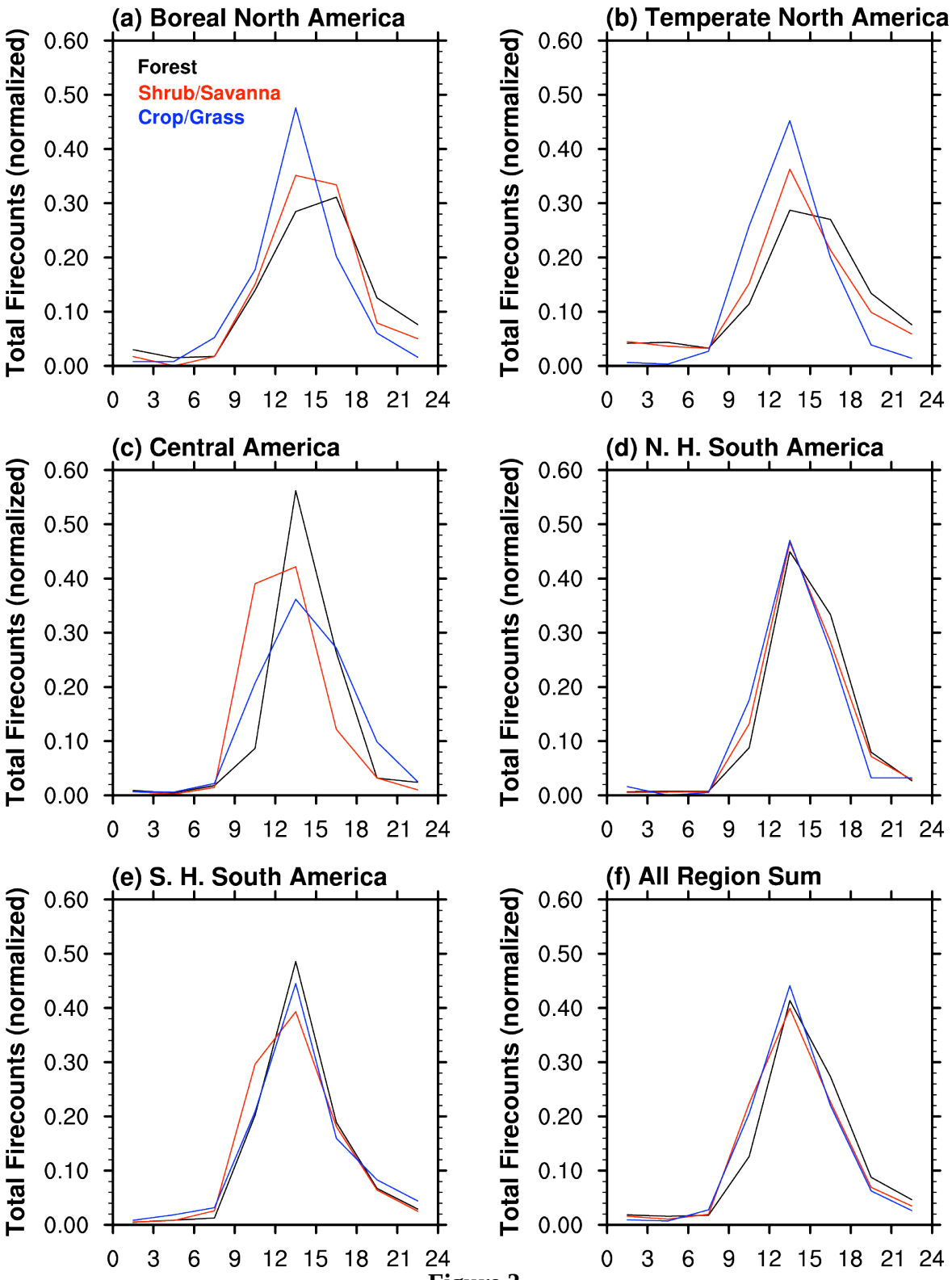
(a) Boreal North America
(b) Temperate North America
(c) Central America
(d) N. H. South America
(e) S. H. South America
(f) All Region Sum
Forest
Shrub/Savanna
Crop/Grass
Total Firecounts (normalized)
0.00
0.10
0.20
0.30
0.40
0.50
0.60
0 3 6 9 12 15 18 21 24

Figure 3.

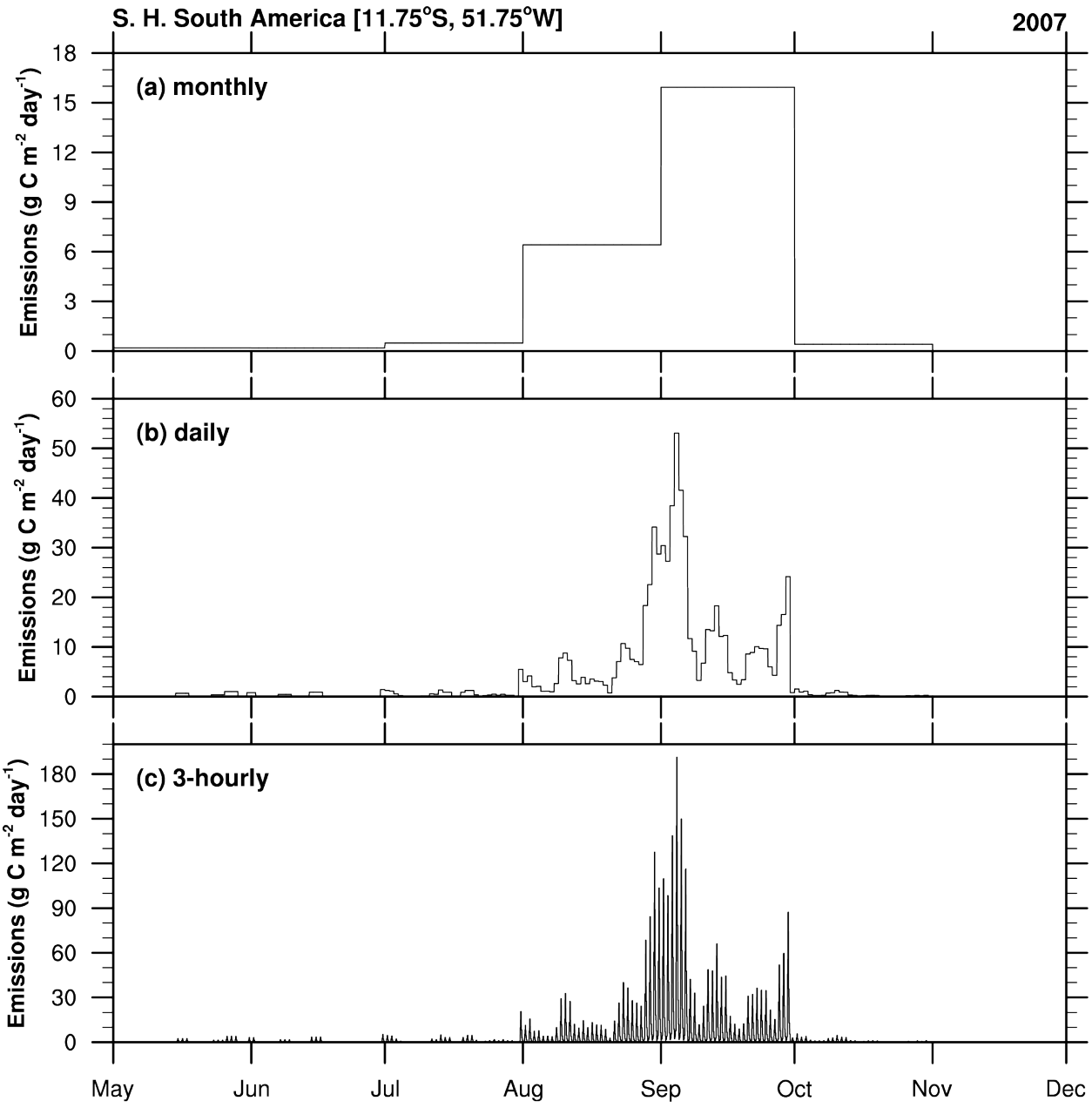
S. H. South America [11.75°S, 51.75°W]
2007
(a) monthly
(b) daily
(c) 3-hourly
Emissions (g C m-2 day-1)
0
3
6
9
12
15
18
10
20
30
40
50
60
90
120
150
180
May
Jun
Jul
Aug
Sep
Oct
Nov
Dec

Figure 4.

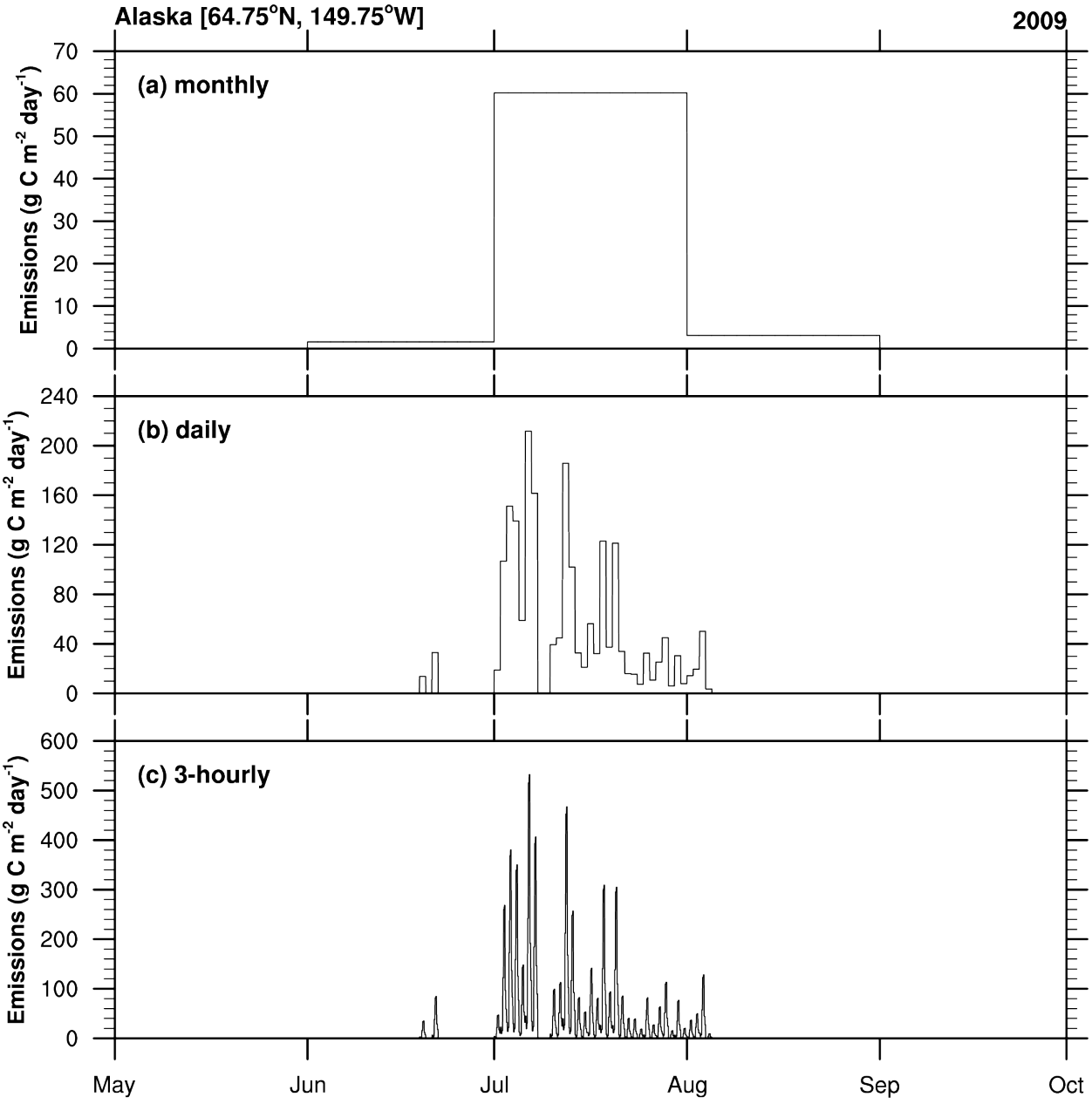
Alaska [64.75°N, 149.75°W]
2009
(a) monthly
(b) daily
(c) 3-hourly
Emissions (g C m-2 day-1)
May
Jun
Jul
Aug
Sep
Oct

Figure 5.

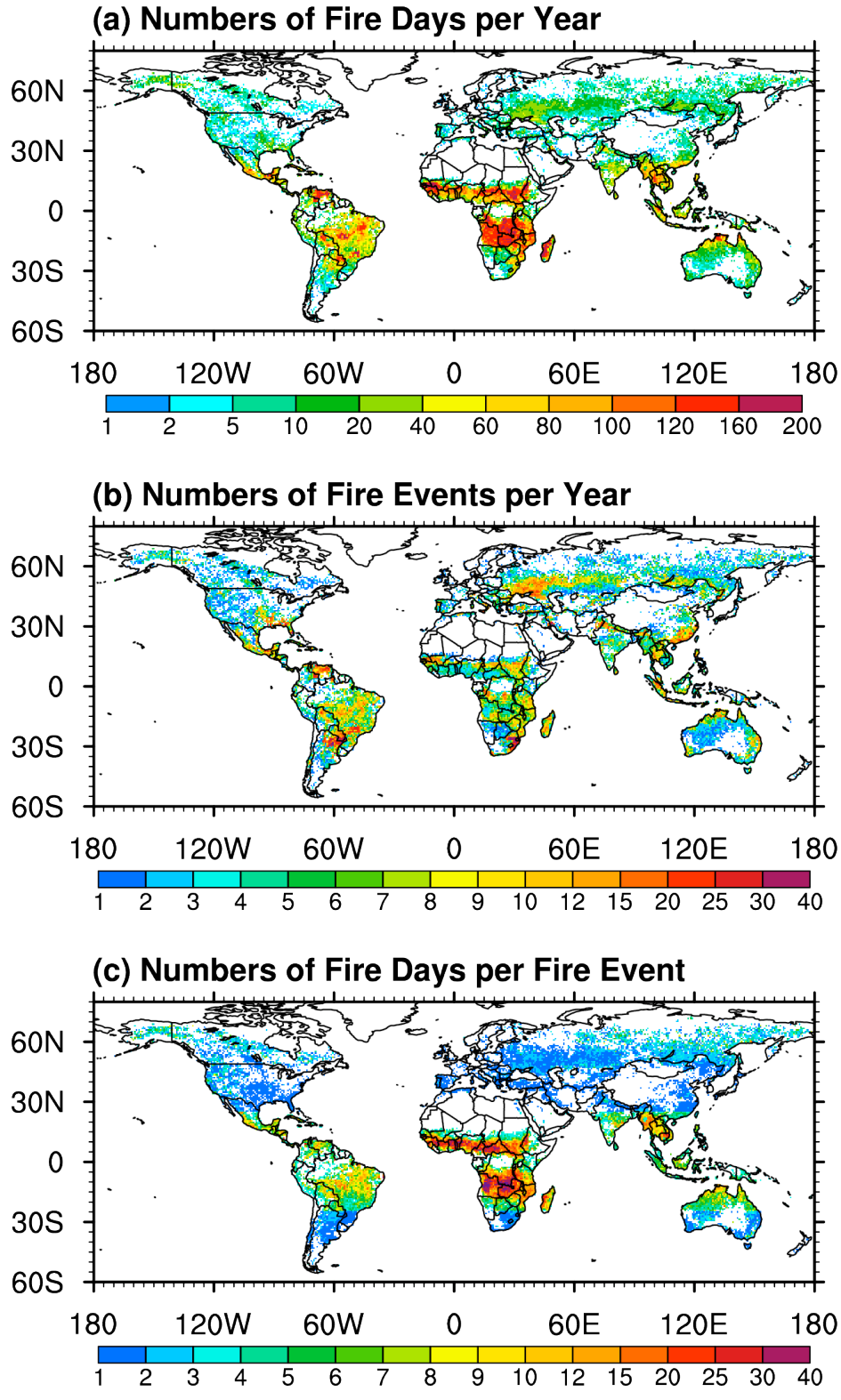
(a) Numbers of Fire Days per Year
60N
30N
0
30S
60S
180
120W
60W
0
60E
120E
180
1 2 5 10 20 40 60 80 100 120 160 200
(b) Numbers of Fire Events per Year
60N
30N
0
30S
60S
180
120W
60W
0
60E
120E
180
1 2 3 4 5 6 7 8 9 10 12 15 20 25 30 40
(c) Numbers of Fire Days per Fire Event
60N
30N
0
30S
60S
180
120W
60W
0
60E
120E
180
1 2 3 4 5 6 7 8 9 10 12 15 20 25 30 40

Figure 6.

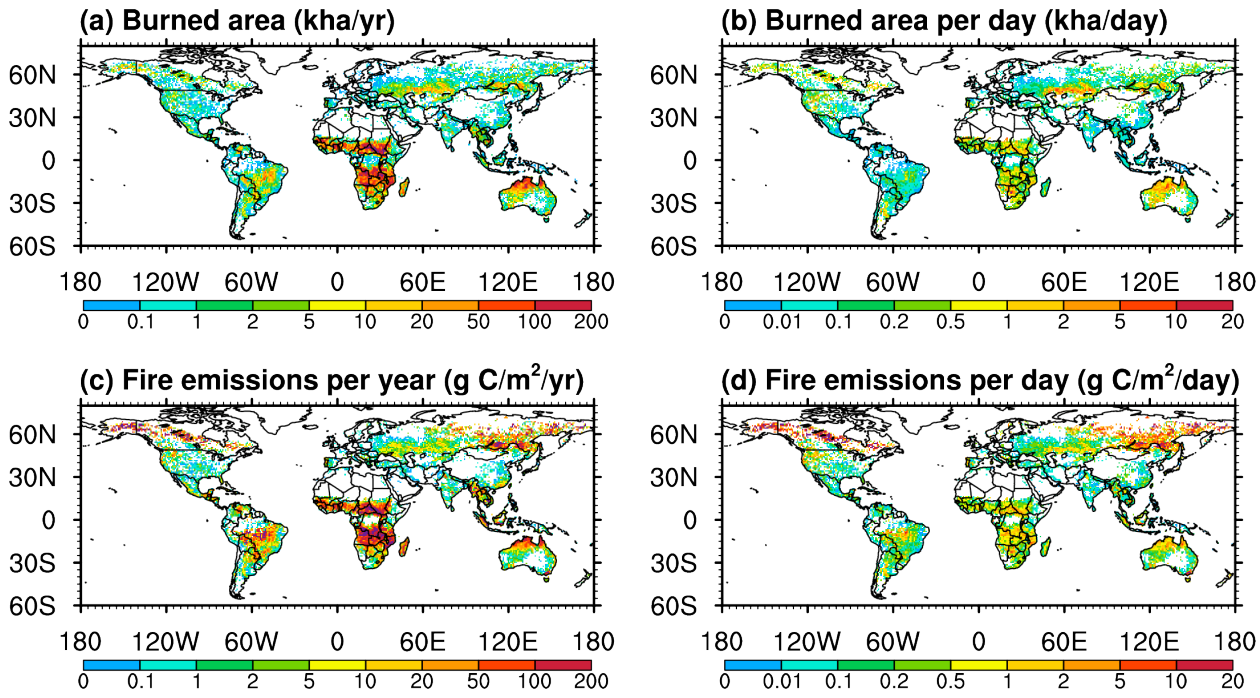
(a) Burned area (kha/yr)
(b) Burned area per day (kha/day)
(c) Fire emissions per year (g C/m2/yr)
(d) Fire emissions per day (g C/m2/day)
60N
30N
0
30S
60S
180 120W 60W 0 60E 120E 180
0 0.1 1 2 5 10 20 50 100 200
0 0.01 0.1 0.2 0.5 1 2 5 10 20

Figure 7.

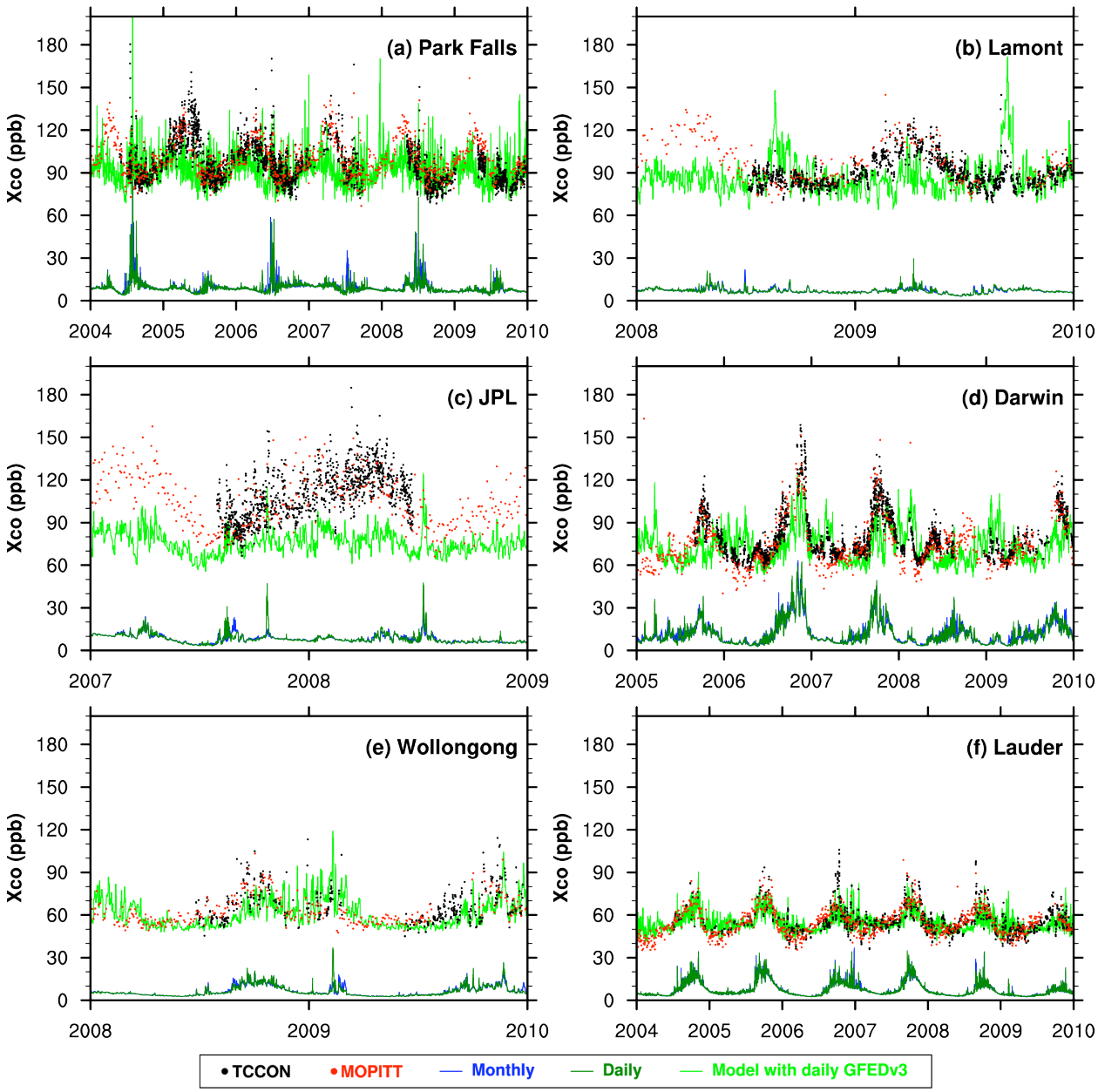
(a) Park Falls
(b) Lamont
(c) JPL
(d) Darwin
(e) Wollongong
(f) Lauder
Xco (ppb)
TCCON
MOPITT
Monthly
Daily
Model with daily GFEDv3

Figure 8.

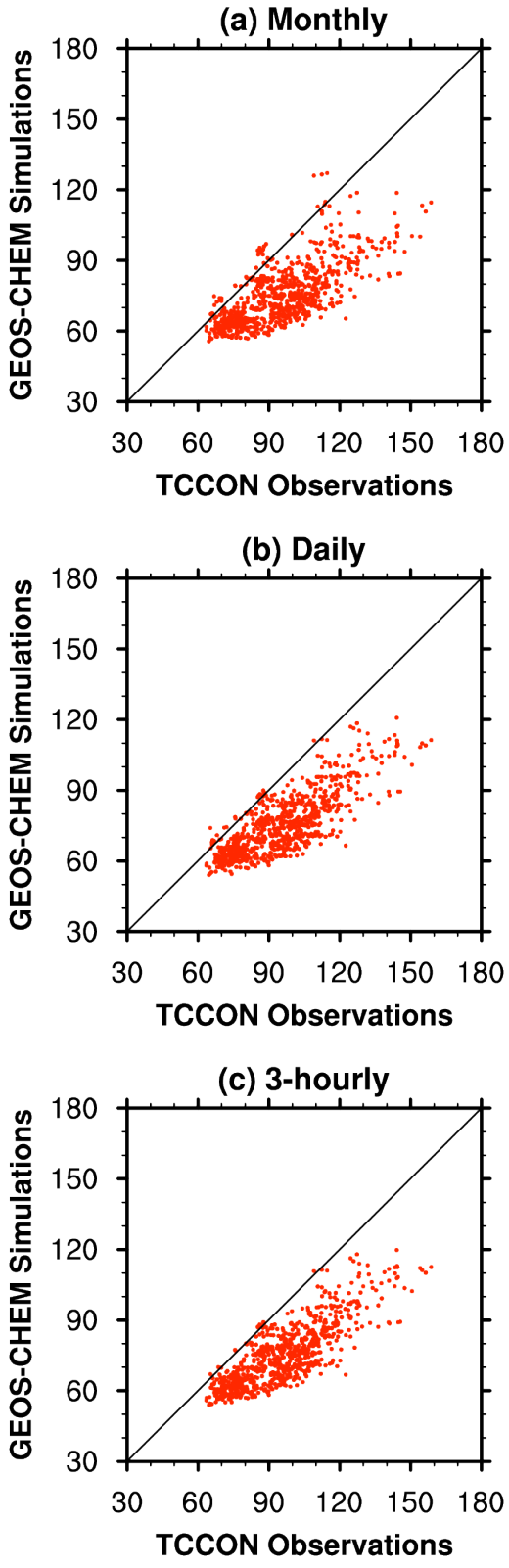
(a) Monthly
GEOS-CHEM Simulations
TCCON Observations
(b) Daily
GEOS-CHEM Simulations
TCCON Observations
(c) 3-hourly
GEOS-CHEM Simulations
TCCON Observations
30
60
90
120
150
180

Figure 9.

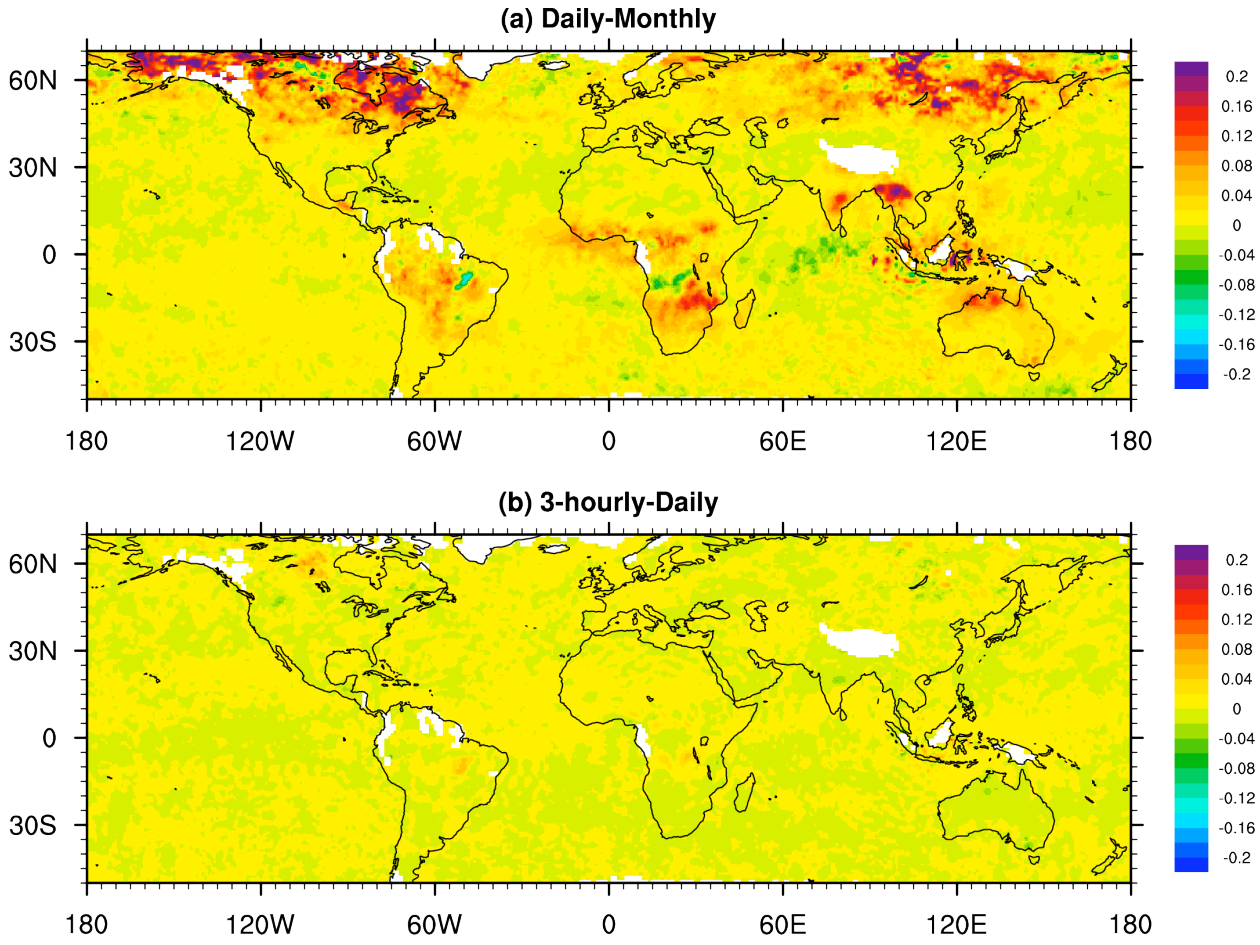
(a) Daily-Monthly
60N
30N
0
30S
180
120W
60W
0
60E
120E
180
0.2
0.16
0.12
0.08
0.04
0
-0.04
-0.08
-0.12
-0.16
-0.2
(b) 3-hourly-Daily
60N
30N
0
30S
180
120W
60W
0
60E
120E
180
0.2
0.16
0.12
0.08
0.04
0
-0.04
-0.08
-0.12
-0.16
-0.2

Figure 10.

Supplementary Materials

Table S1. Ratios of active fire counts (including both day and night overpasses) from MODIS sensors on Aqua and Terra satellites.

Figure S1. Daily fire counts from GOES (upper panel), Aqua and Terra (middle panel), and Aqua and Terra with a 3-day centered mean smoothing filter (bottom panel) for a 0.5° grid cell at 11.75°S, 51.75°W in southern South America during 2007. In the middle and bottom panels, the adjusted time series was constructed by multiplying Terra daily active fires by regional factors shown in Table S1 prior to taking the Aqua and Terra sum. This was done to weight the contributions from Terra equally to those from Aqua (and thus accounting for differences in satellite overpass times).

Figure S2. The same as Figure S1, but for a 0.5° grid cell in interior Alaska at 64.75°N, 149.75°W during the summer of 2009.

Figure S3. Diurnal cycles of fires based for 3-hour intervals derived using GOES active fire counts. The different diurnal cycles were constructed only using grid cells at a 0.05°×0.05° resolution each within region that had 80% or more coverage by each vegetation type.

Figure S4. Total burned area (Mha/month) for each region for each of the aggregated vegetation type used here to construct monthly mean diurnal cycles.

Figure S5. Percent contribution of different aggregated vegetation types to total monthly burned area within each region.

Figure S6. Geographic regions used in the analysis of GFED fire emissions.

Figure S7. Vertical profiles of the averaging kernels for different solar zenith angles at (a) Darwin and (b) Lamont TCCON stations.

Table S1. Ratios of active fire counts (including both day and night overpasses) from MODIS sensors on Aqua and Terra satellites.

Region	Ratio of active fires (Aqua/Terra) by year[1]							mean	σ
	2003	2004	2005	2006	2007	2008	2009		
BONA	0.97	0.77	0.74	0.94	0.90	0.96	0.80	0.87	0.10
TENA	1.28	1.37	1.23	1.18	1.16	1.19	1.34	1.25	0.08
CEAM	1.45	1.37	1.55	1.40	1.33	1.39	1.44	1.42	0.07
NHSA	1.52	1.55	1.55	1.56	1.46	1.41	1.46	1.50	0.06
SHSA	2.04	1.83	1.71	1.85	1.73	1.78	1.73	1.81	0.12
EURO	1.14	1.00	1.16	1.08	1.09	1.06	1.11	1.09	0.05
MIDE	0.82	0.84	0.87	0.86	0.89	0.89	0.84	0.86	0.03
NHAF	2.45	2.21	2.19	2.24	2.23	2.37	2.41	2.30	0.11
SHAF	3.20	3.27	3.30	3.34	3.23	3.25	3.44	3.29	0.08
BOAS	0.99	1.01	1.00	0.96	1.07	1.09	0.97	1.01	0.05
CEAS	1.20	1.12	1.08	1.02	1.04	1.04	1.10	1.09	0.06
SEAS	3.33	3.18	3.03	3.35	3.04	3.00	2.97	3.13	0.16
EQAS	2.43	2.31	1.77	1.93	2.52	2.49	1.76	2.17	0.34
AUST	1.33	1.28	1.49	1.30	1.17	1.44	1.35	1.34	0.11

1. These ratios were obtained by first computing the sum of all active fires from Terra and Aqua within a year for each region and then in a second step calculating the ratio between active fires from the two satellites.

Table S2 Sources of emissions for CO simulations for the GEOS-Chem v8-01-02 model simulations described in the main text

Source	Amount (Tg CO/yr)	Reference
Fossil fuel emissions	370	*Streets et al.* [2006]
Biomass burning	325	*van der Werf et al.* [2010]
Biofuels	189	*Yevich and Logan* [2003]
CH_4 oxidation	905	*DeMore et al.* [1997]
Biogenic compound oxidation	443	*Guenther et al.* [2006]
Total:	2232	

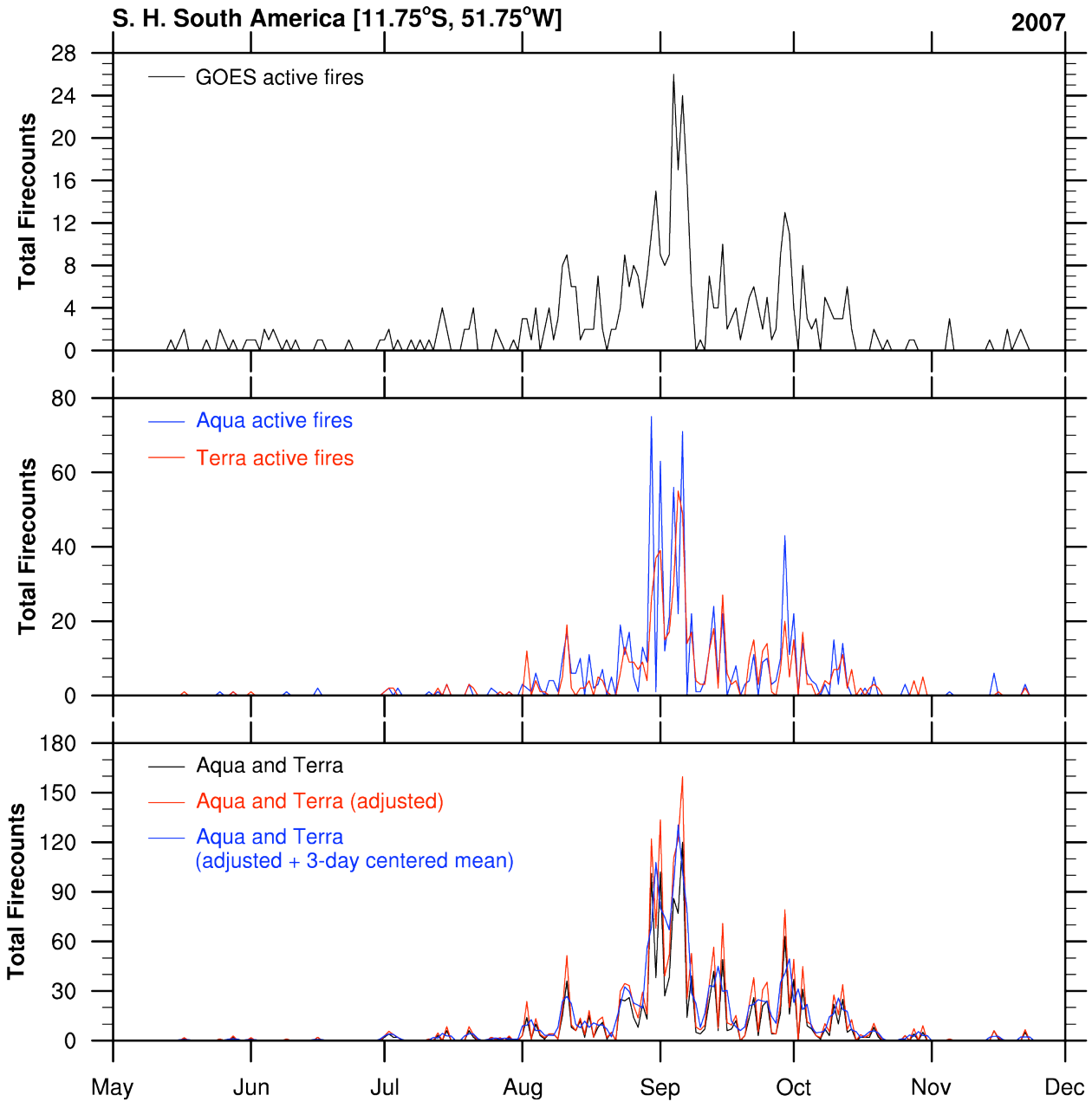
S. H. South America [11.75°S, 51.75°W]
2007
GOES active fires
Total Firecounts
Aqua active fires
Terra active fires
Aqua and Terra
Aqua and Terra (adjusted)
Aqua and Terra
(adjusted + 3-day centered mean)
May
Jun
Jul
Aug
Sep
Oct
Nov
Dec

Figure S1.

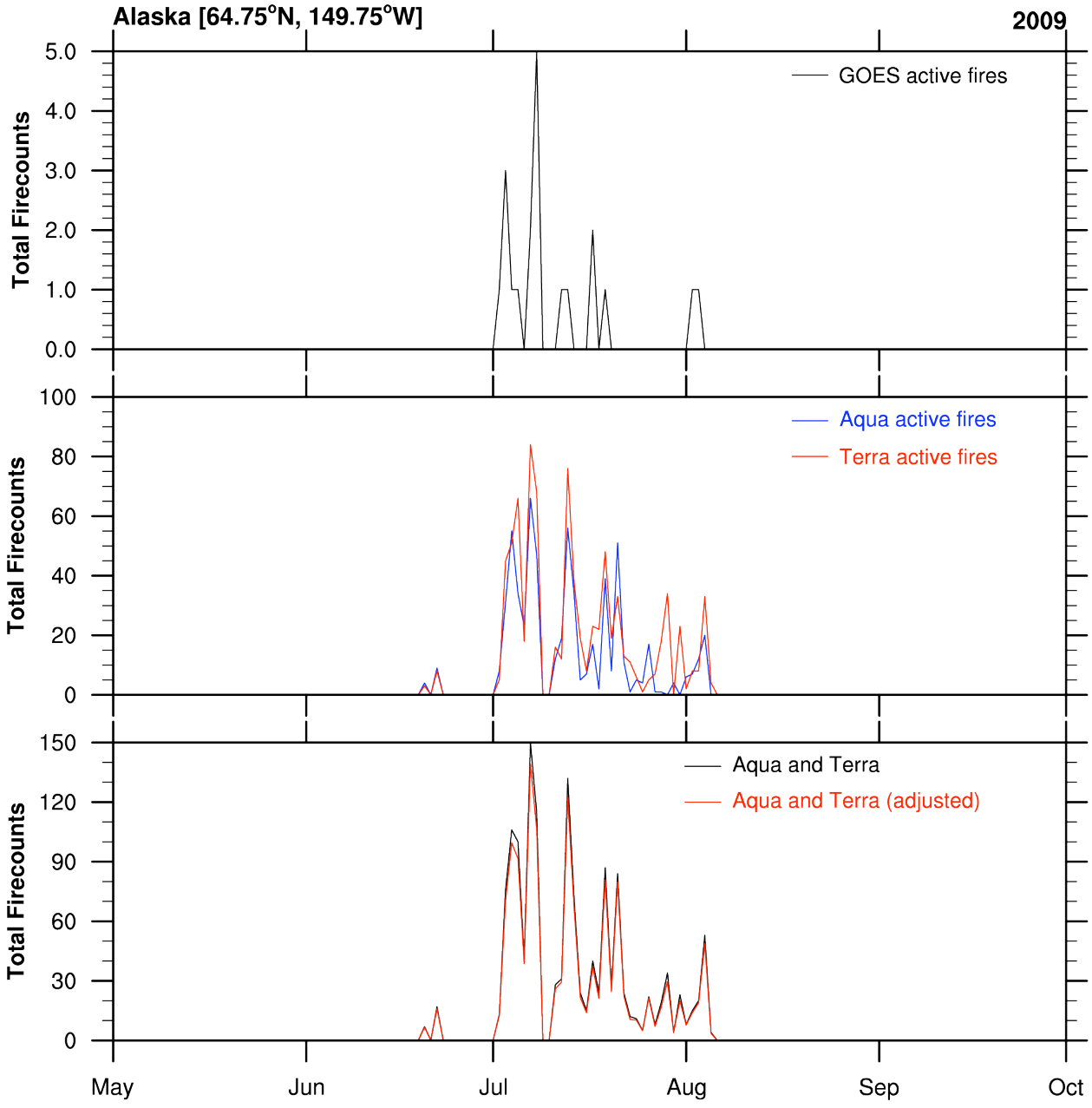
Alaska [64.75°N, 149.75°W]
2009
GOES active fires
Aqua active fires
Terra active fires
Aqua and Terra
Aqua and Terra (adjusted)
Total Firecounts
5.0
4.0
3.0
2.0
1.0
0.0
100
80
60
40
20
0
150
120
90
60
30
0
May
Jun
Jul
Aug
Sep
Oct

Figure S2.

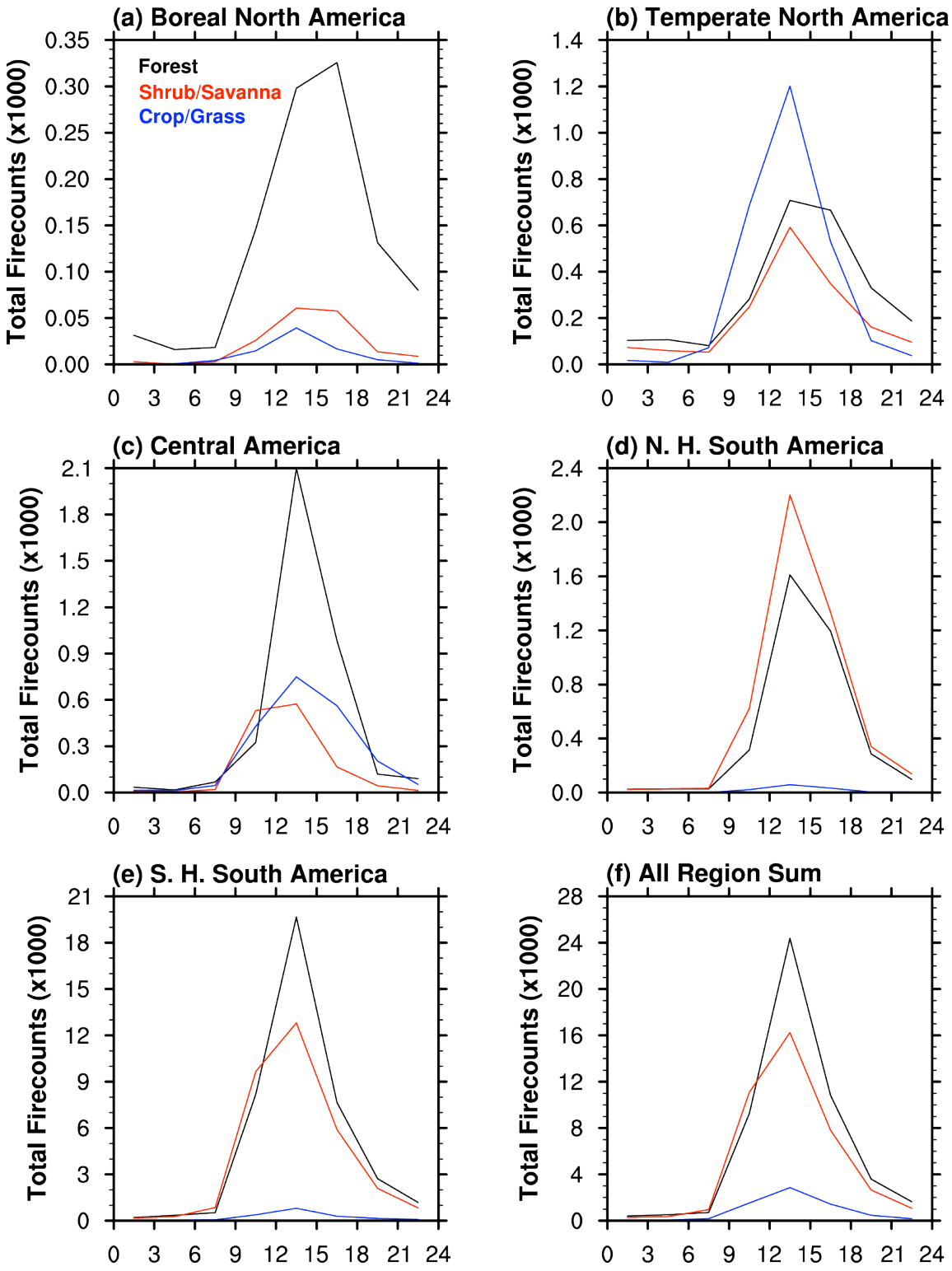
(a) Boreal North America
Forest
Shrub/Savanna
Crop/Grass
Total Firecounts (x1000)
0.35
0.30
0.25
0.20
0.15
0.10
0.05
0.00
0 3 6 9 12 15 18 21 24
(b) Temperate North America
Total Firecounts (x1000)
1.4
1.2
1.0
0.8
0.6
0.4
0.2
0.0
0 3 6 9 12 15 18 21 24
(c) Central America
Total Firecounts (x1000)
2.1
1.8
1.5
1.2
0.9
0.6
0.3
0.0
0 3 6 9 12 15 18 21 24
(d) N. H. South America
Total Firecounts (x1000)
2.4
2.0
1.6
1.2
0.8
0.4
0.0
0 3 6 9 12 15 18 21 24
(e) S. H. South America
Total Firecounts (x1000)
21
18
15
12
9
6
3
0
0 3 6 9 12 15 18 21 24
(f) All Region Sum
Total Firecounts (x1000)
28
24
20
16
12
8
4
0
0 3 6 9 12 15 18 21 24

Figure S3.

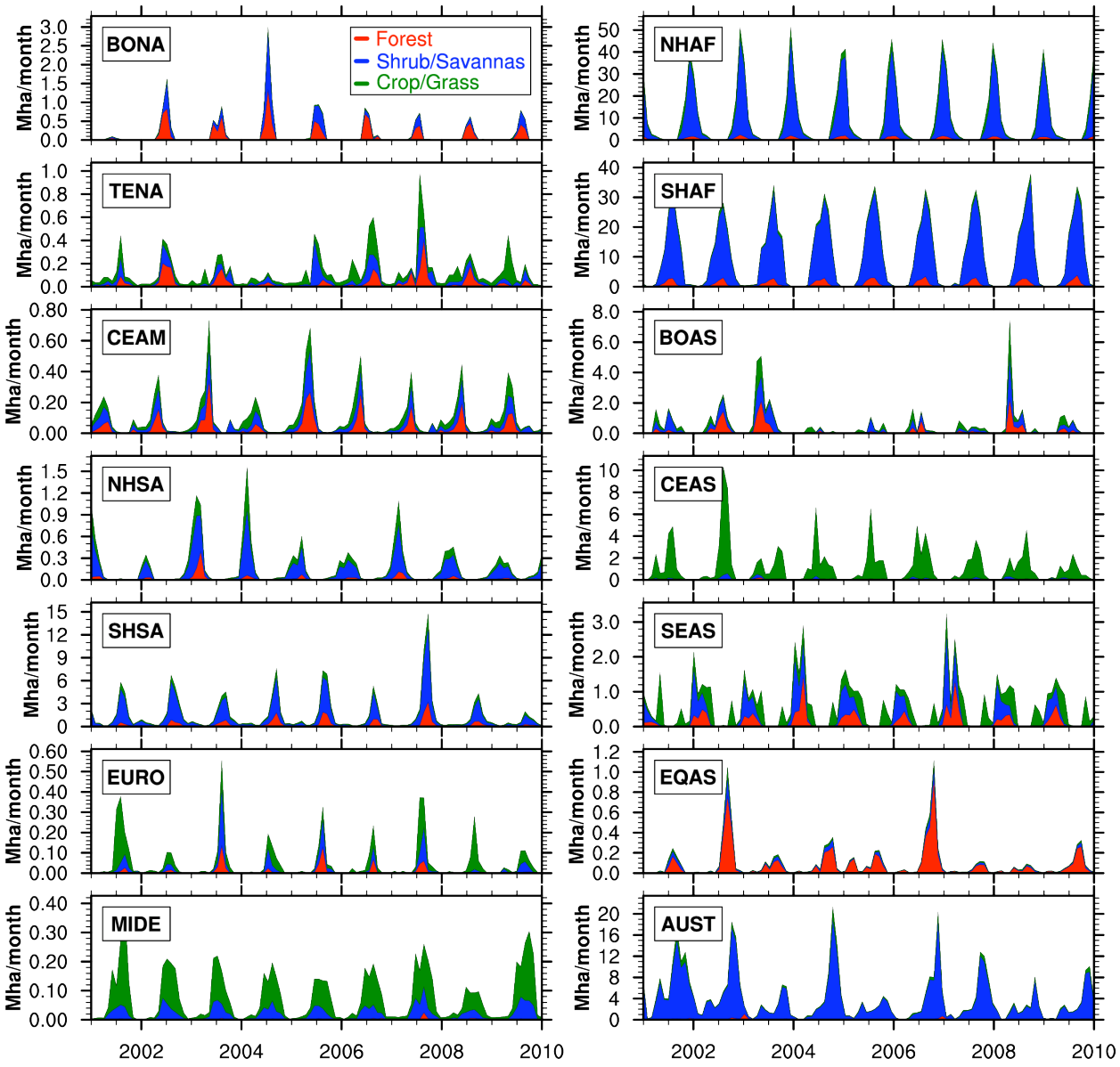
BONA
Forest
Shrub/Savannas
Crop/Grass
NHAF
TENA
SHAF
CEAM
BOAS
NHSA
CEAS
SHSA
SEAS
EURO
EQAS
MIDE
AUST
Mha/month
2002
2004
2006
2008
2010

Figure S4.

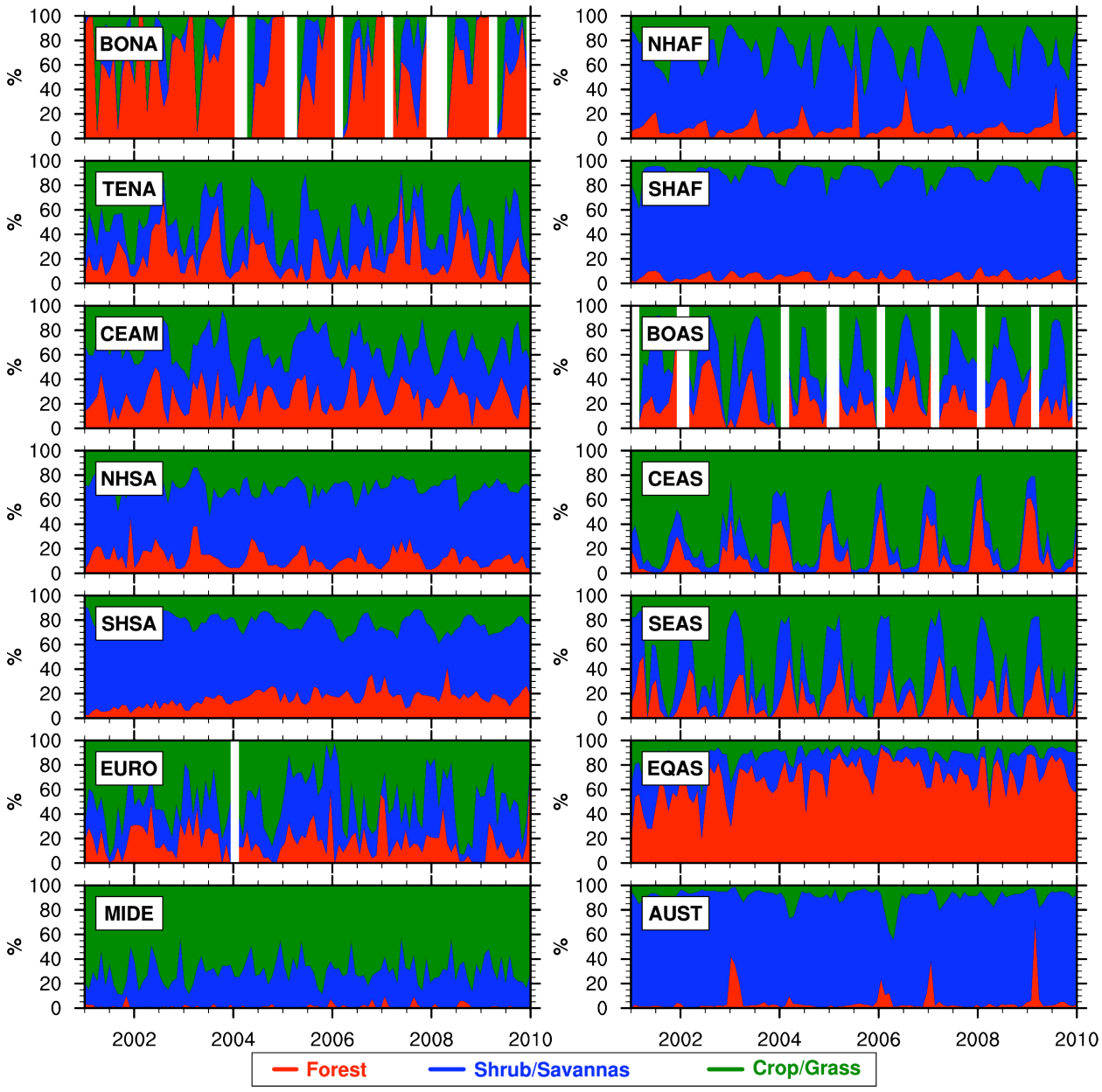
BONA
NHAF
TENA
SHAF
CEAM
BOAS
NHSA
CEAS
SHSA
SEAS
EURO
EQAS
MIDE
AUST
%
0
20
40
60
80
100
2002
2004
2006
2008
2010
Forest
Shrub/Savannas
Crop/Grass

Figure S5

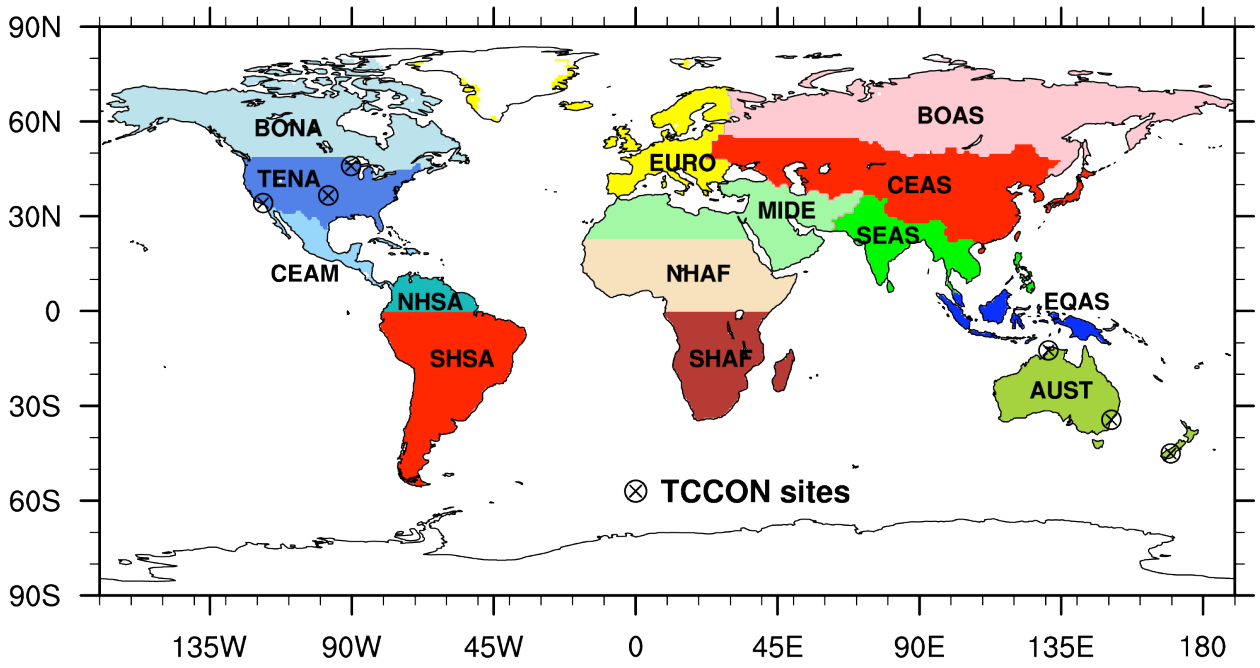
90N
60N
30N
0
30S
60S
90S
135W
90W
45W
0
45E
90E
135E
180
BONA
TENA
CEAM
NHSA
SHSA
EURO
BOAS
CEAS
MIDE
SEAS
NHAF
SHAF
EQAS
AUST
⊗ TCCON sites

Figure S6.

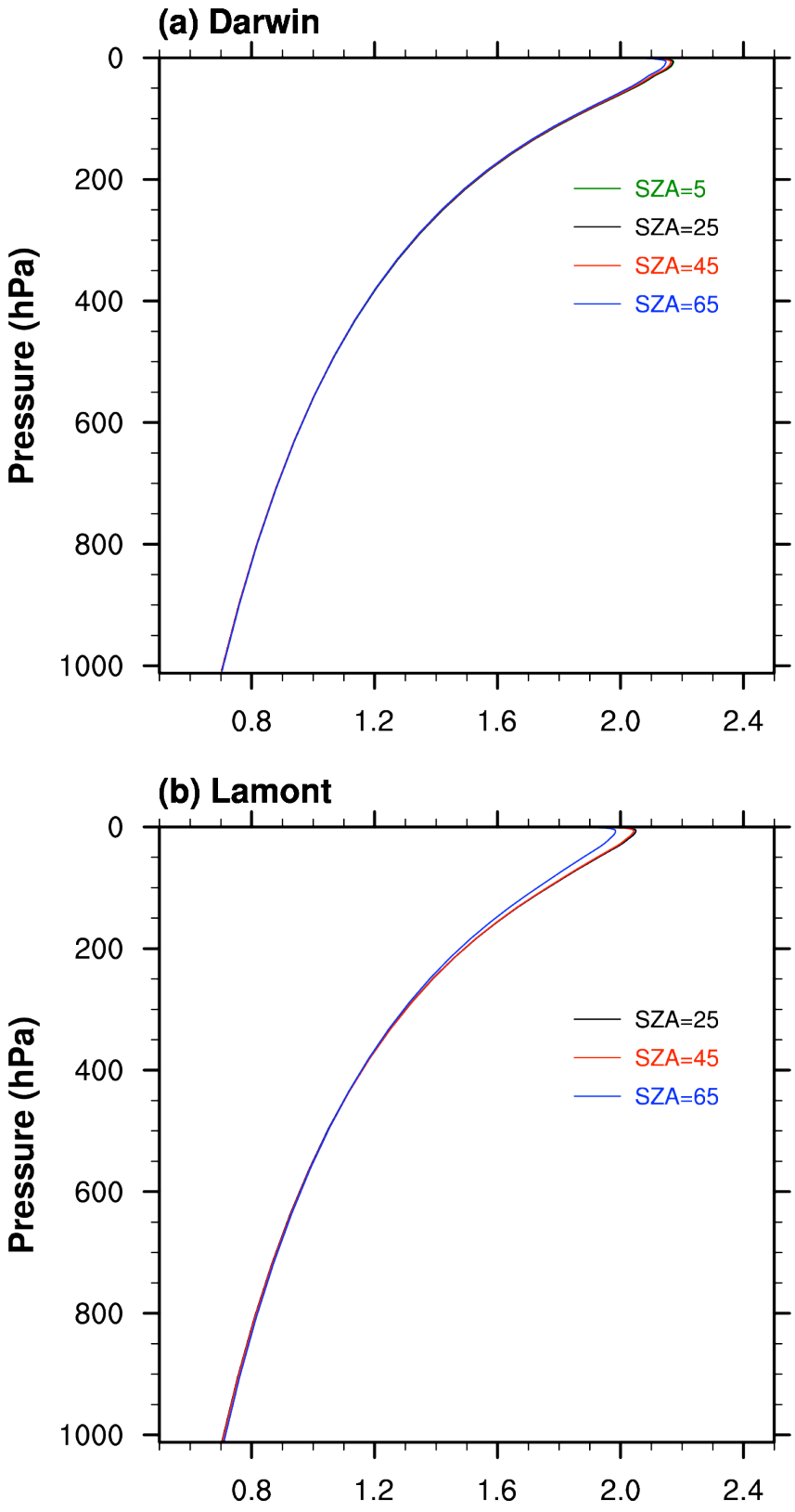
(a) Darwin
Pressure (hPa)
0
200
400
600
800
1000
0.8
1.2
1.6
2.0
2.4
SZA=5
SZA=25
SZA=45
SZA=65
(b) Lamont
Pressure (hPa)
0
200
400
600
800
1000
0.8
1.2
1.6
2.0
2.4
SZA=25
SZA=45
SZA=65

Figure S7.